Chemical Geology 504 (2019) 123–135

Contents lists available at ScienceDirect

Chemical Geology

journal homepage: www.elsevier.com/locate/chemgeo

Solubility of the hydrated Mg-carbonates nesquehonite and dypingite from 5 to 35 °C: Implications for CO_2 storage and the relative stability of Mg-carbonates

Anna L. Harrison[a,b,*,1], Vasileios Mavromatis[b,c], Eric H. Oelkers[a,b], Pascale Bénézeth[b]

[a] Department of Earth Sciences, University College London, Gower Street, WC1E 6BT London, United Kingdom
[b] Geoscience and Environment Toulouse (GET), CNRS, UMR 5563, Observatoire Midi-Pyrénées, 14 Avenue Edouard Belin, 31400 Toulouse, France
[c] Institute of Applied Geosciences, Graz University of Technology, Rechbauerstrasse 12, 8010 Graz, Austria

ARTICLE INFO

Editor: B Kamber

Keywords:
Mg-carbonates
CO_2 sequestration
Mineral solubility
Ultramafic mineral weathering
Mineral phase transformation
Dissolution-reprecipitation
Dypingite
Nesquehonite

ABSTRACT

Hydrated Mg-carbonate minerals form during the weathering of ultramafic rocks, and can be used to store atmospheric CO_2 to help combat greenhouse gas-fueled climate change. Optimization of engineered CO_2 storage and prediction of the composition and stability of Mg-carbonate phase assemblages in natural and engineered ultramafic environments requires knowledge of the solubility of hydrated Mg-carbonate phases, and the transformation pathways between these metastable phases. In this study, we evaluate the solubility of nesquehonite [$MgCO_3{\cdot}3H_2O$] and dypingite [$Mg_5(CO_3)_4(OH)_2{\cdot}$(5 or 8)$H_2O$] and the transformation from nesquehonite to dypingite between 5 °C and 35 °C, using constant-temperature, batch-reactor experiments. The logarithm of the solubility product of nesquehonite was determined to be: -5.03 ± 0.13, -5.27 ± 0.15, and -5.34 ± 0.04 at 5 °C, 25 °C, and 35 °C, respectively. The logarithm of the solubility product of dypingite was determined to be: -34.95 ± 0.58 and -36.04 ± 0.31 at 25 °C and 35 °C, respectively, with eight waters of hydration. This is the first reported dypingite solubility product. The transformation from nesquehonite to dypingite was temperature-dependent, and was complete within 57 days at 25 °C, and 20 days at 35 °C, but did not occur during experiments of 59 days at 5 °C. This phase transformation appeared to occur via a dissolution-reprecipitation mechanism; external nesquehonite crystal morphology was partially maintained during the phase transformation at 25 °C, but was eradicated at 35 °C. Together, our results facilitate the improved evaluation of Mg-carbonate mineral precipitation in natural and engineered ultramafic mineral weathering systems that sequester CO_2, and for the first time allow assessment of the saturation state of dypingite in aqueous solutions.

1. Introduction

The largest proportion of carbon in Earth's crust is bound in carbonate minerals, where it is stable over millennia (Lackner, 2003; Sundquist, 1993). The engineered storage of anthropogenic CO_2 in carbonate minerals is therefore sought to offset greenhouse gas emissions and mitigate climate change (Kelemen and Matter, 2008; Lackner et al., 1995; Matter et al., 2016; Oelkers and Cole, 2008; Power et al., 2013a, b). Carbonate mineral formation during the weathering of silicates and hydroxides is a naturally occurring process, known as carbon mineralization; this process can be enhanced artificially to store CO_2. Several engineered carbon mineralization approaches have been studied at the laboratory and/or pilot-scale, including injection of CO_2 into subsurface basaltic or ultramafic rock (Gislason and Oelkers, 2014; Kelemen and Matter, 2008; Matter et al., 2016; Power et al., 2013a, b), passive or accelerated carbonation of ultramafic mine waste rock and tailings (Assima et al., 2012, 2014a, b, c; Bea et al., 2012; Beinlich and Austrheim, 2012; Harrison et al., 2013a, b, 2015, 2016; McCutcheon et al., 2017, 2015; Oskierski et al., 2013; Power et al., 2010, 2014a; Pronost et al., 2011, 2012; Wilson et al., 2006, 2009a, b, 2011, 2014; Gras et al., 2017), and accelerated mineralization in high pressure/high temperature ex situ reactors (Gerdemann et al., 2007; Lackner et al., 1995). Enhanced weathering is a related approach that aims primarily to sequester CO_2 in dissolved form, but can also induce carbonate

* Corresponding author at: Department of Earth Sciences, University College London, Gower Street, WC1E 6BT London, United Kingdom.
E-mail addresses: anna.harrison@queensu.ca (A.L. Harrison), vasileios.mavromatis@get.omp.eu (V. Mavromatis), eric.oelkers@get.omp.eu (E.H. Oelkers), pascale.benezeth@get.omp.eu (P. Bénézeth).
[1] Present address: Department of Geological Sciences and Geological Engineering and School of Environmental Studies, Queen's University, K7L 3N6 Kingston, Canada.

https://doi.org/10.1016/j.chemgeo.2018.11.003
Received 11 July 2018; Received in revised form 19 October 2018; Accepted 11 November 2018
Available online 19 November 2018
0009-2541/ © 2018 Elsevier B.V. All rights reserved.

precipitation. It entails spreading fine-grained mafic or ultramafic rock in natural weathering environments to artificially enhance natural weathering (Hartmann et al., 2013; Montserrat et al., 2017; Renforth, 2012; Rigopoulos et al., 2018; Schuiling and Krijgsman, 2006). Estimation of the CO_2 storage security of these approaches requires knowledge of the stability, solubility, and formation pathways of the carbonate mineral products that store the CO_2. The relative stability and solubility of several Mg-carbonates has been investigated (Ballirano et al., 2013; Bénézeth et al., 2011, 2018; Berninger et al., 2014; Canterford et al., 1984; Gautier et al., 2014; Hänchen et al., 2008; Hopkinson et al., 2008, 2012; Königsberger et al., 1999; Kristova et al., 2014; Langmuir, 1965; Xiong, 2011; Xiong and Lord, 2008; Zhang et al., 2006). In general, the stability of Mg-carbonates increases from more to less hydrated phases, in the order: lansfordite < nesquehonite < dypingite < hydromagnesite < magnesite (Canterford et al., 1984; Langmuir, 1965). Due to the strong hydration of aqueous Mg, the formation of anhydrous magnesite [$MgCO_3$], is kinetically inhibited at low temperatures, and is rarely observed to form on laboratory timescales at temperature less than 60 °C (Hänchen et al., 2008; Power et al., 2017; Saldi et al., 2009, 2012). For example, Gautier et al. (2014) demonstrate a 2.5-fold greater growth rate constant for hydromagnesite [$Mg_5(CO_3)_4(OH)_2{\cdot}4H_2O$] compared to magnesite at 90 °C. Thus, ultramafic weathering at the Earth's near-surface is dominated by hydrated Mg-carbonate formation (Lin et al., 2017; Power et al., 2014b; Shirokova et al., 2013), and engineered CO_2 storage efforts at near-Earth's surface temperatures will also tend to form hydrated Mg-carbonates. However, observed mineral assemblages in the field and in laboratory experiments reveal that multiple hydrated magnesium carbonate phases often co-exist, with the more-hydrated phases frequently acting as transient precursors to the more stable, less-hydrated phases (Ballirano et al., 2013; Davies and Bubela, 1973; Harrison et al., 2015, 2016; Hopkinson et al., 2008, 2012; Power et al., 2014b; Wilson et al., 2009a). The multitude of potential metastable hydrated phases complicates prediction of Mg-carbonate formation and thus the stability of the CO_2-storing phase (Hänchen et al., 2008; Hopkinson et al., 2008, 2012; Königsberger et al., 1999; Kristova et al., 2014; Montes-Hernandez et al., 2012). To reduce some of the ambiguity in prediction of Mg-carbonate mineral formation under various conditions, in this study we determine the solubility of nesquehonite [$MgCO_3{\cdot}3H_2O$] and dypingite [$Mg_5(CO_3)_4(OH)_2{\cdot}$(5 or 8)$H_2O$], two commonly observed products of carbon mineralization in ultramafic materials (Assima et al., 2012, 2014c; Bea et al., 2012; Beinlich and Austrheim, 2012; Boschi et al., 2009; Chaka et al., 2016; Felmy et al., 2012; Garcia del Real et al., 2016; Gras et al., 2017; Harrison et al., 2013a, 2015, 2016, 2017; Highfield et al., 2016; Hövelmann et al., 2012; Kristova et al., 2014; Loring et al., 2012; McCutcheon et al., 2016, 2017; Montes-Hernandez et al., 2012; Power et al., 2013a, b, 2014b; Pronost et al., 2011; Schaef et al., 2011, 2013; Wilson et al., 2006, 2009a, b, 2011, 2014; Zhao et al., 2010), and the transformation process that converts nesquehonite to dypingite. Both nesquehonite and dypingite are readily formed during reaction of Mg-rich minerals with CO_2 at ambient temperatures, with nesquehonite tending to form at greater than atmospheric pCO_2 or evaporative conditions (Harrison et al., 2013a; Königsberger et al., 1999; Power et al., 2007; Schaef et al., 2011; Xiong and Lord, 2008; Zhao et al., 2010), and dypingite favored under atmospheric pCO_2 (~400 ppm) and microbially-mediated conditions (Harrison et al., 2013a; Mavromatis et al., 2012; McCutcheon et al., 2016; Power et al., 2007; Shirokova et al., 2013; Wilson et al., 2010). In addition to their natural occurrence and use for CO_2 storage, hydrated Mg-carbonates have prompted interest due to their potential formation in engineered $Mg(OH)_2$/MgO barriers for nuclear waste storage (Xiong, 2011; Xiong and Lord, 2008), and the precipitation of nesquehonite from $MgCl_2$ brines has been investigated as a way to exploit Mg resources from salt lakes (Cheng and Li, 2009; Cheng et al., 2009; Dong et al., 2008; Wang et al., 2008), and as a precursor for high purity MgO production (Cheng et al., 2009; Wang and Li, 2012). This broad interest in nesquehonite has inspired a number of studies regarding its thermal stability (Ballirano et al., 2010; Hales et al., 2008; Jauffret et al., 2015; Lanas and Alvarez, 2004; Morgan et al., 2015; Vágvölgyi et al., 2008), nucleation kinetics (Cheng and Li, 2010; Zhao et al., 2013), its tendency for solid-solution with transition metals (Hamilton et al., 2016), and the impacts of temperature, saturation state, and fluid composition on nucleation and crystal morphology and size (Cheng et al., 2009; Ding et al., 2016; Wang et al., 2008; Zhang et al., 2006). Robie and Hemingway (1972, 1973) determined its standard heat capacity, standard entropy, and standard enthalpy of formation. Although several solubility studies of nesquehonite have been conducted both experimentally and theoretically, they report differing results, or in some cases do not report a solubility product, instead reporting total aqueous Mg or C concentrations (*c.f.*, Dong et al., 2008, 2009; Hostetler, 1964; Kazakov et al., 1959; Kline, 1929; Königsberger et al., 1999; Langmuir, 1965; Wang and Li, 2012). On the other hand, dypingite solubility remains undetermined, despite its common occurrence in natural and engineered ultramafic weathering environments (Power et al., 2013a and references therein). Dypingite can be a precursor for the formation of hydromagnesite (Davies and Bubela, 1973; Hopkinson et al., 2008, 2012; Sutradhar et al., 2011), a mineral that securely stores CO_2 over tens of thousands of years at Earth's surface conditions (e.g., Power et al., 2009, 2014b). The process by which the metastable Mg-carbonates transform from less to more stable phases is also an important control on the isotopic signature of the carbonate minerals, which can be used to trace CO_2 cycling and sequestration processes (Beinlich and Austrheim, 2012; Falk et al., 2016; Gras et al., 2017; Harrison et al., 2013a, 2016; Mervine et al., 2014; Oskierski et al., 2013, 2016; Power et al., 2007, 2014b; Shirokova et al., 2013; Wilson et al., 2009a, 2010, 2011, 2014). Similarly, the mobility of toxic metals that can be incorporated in nesquehonite (Hamilton et al., 2016) will be controlled in part by the efficiency and mechanism of Mg-carbonate phase transformations.

The goals of the present study were to 1) determine the solubility of nesquehonite and dypingite at conditions relevant to natural and engineered CO_2-driven weathering, and 2) assess the nesquehonite-dypingite transformation pathway and the implications for CO_2 storage.

2. Methods

2.1. Nesquehonite and dypingite synthesis

Nesquehonite was synthesized according to a modified method of Robie and Hemingway (1972), whereby 200 mL of an aqueous 1.8 mol/L K_2CO_3 solution (reagent grade K_2CO_3) was slowly added to a 1000 mL glass beaker containing 200 mL of 1.8 mol/L aqueous $MgCl_2$ (NormaPur $MgCl_2{\cdot}6H_2O$). The beaker was then covered with a watch glass to permit some exchange with laboratory air but limit evaporation and dust inputs. A white gel-like precipitate was formed immediately upon mixing of the two solutions. This precipitate was allowed to age in the solution for five days at ambient temperature (~22 °C) after which the slurry was vacuum-filtered and rinsed multiple times with distilled, de-ionized water. The precipitate was then dried at ambient temperature for ~3 days. Once dry, the precipitate was gently disaggregated using an agate mortar and pestle, and stored in a desiccator prior to analysis and use in experiments. The nesquehonite was made in two separate batches due to the large quantity required, and each was used in separate experimental runs; a short-term experiment (nesquehonite batch 1), and a long-term experiment (nesquehonite batch 2). The long-term experiment was conducted subsequent to the short-term experiment to capture the complete conversion of nesquehonite to dypingite. Dypingite was synthesized via transformation of the synthetic nesquehonite within the experiments. The experimental conditions are described in more detail in Section 2.2.

The synthetic nesquehonite was characterized using X-ray diffraction (XRD) and Fourier transform infrared spectroscopy (FTIR), which confirmed the presence of only nesquehonite in the initial solids used in the

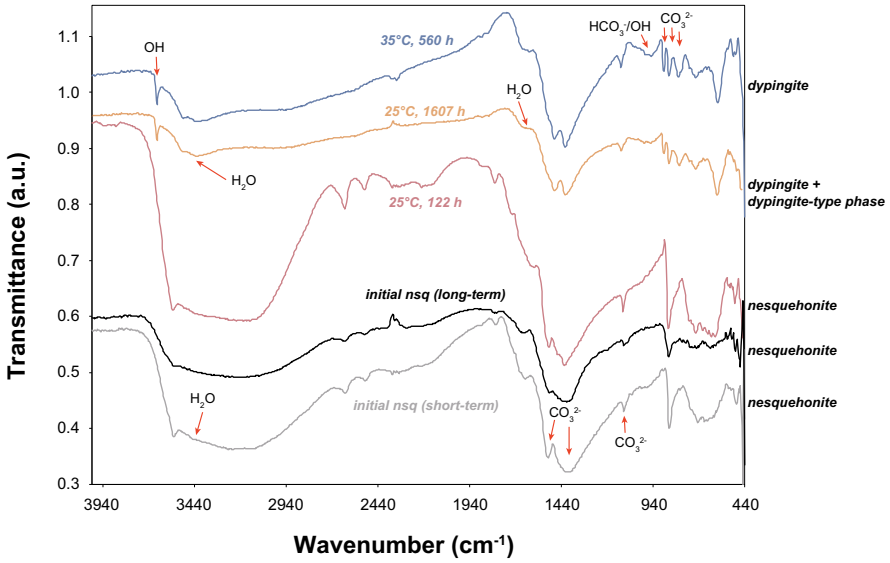

Fig. 1. Fourier transform infrared spectroscopy (FTIR) data for selected samples. Spectra are offset along y-axis. Intensities on the y-axis are in arbitrary units (a.u.).

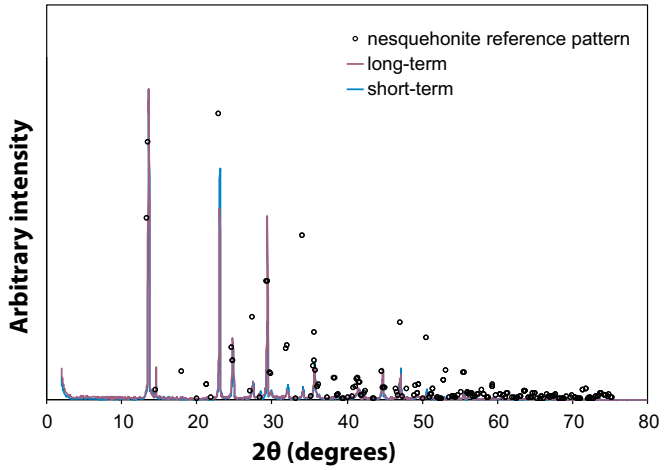

Fig. 2. X-ray diffraction patterns of initial nesquehonite used in the short-term (blue line) and long-term (purple line) experiments. The location of peaks in the nesquehonite reference pattern are indicated by black circles. (For interpretation of the references to colour in this figure legend, the reader is referred to the web version of this article.)

experiments (Figs. 1 and 2). The empirical formula of nesquehonite has been debated, and is sometimes reported as $[Mg(OH)(HCO_3)\cdot 2H_2O]$ (Frost and Palmer, 2011). However, the FTIR spectra collected from the samples in this study were more consistent with the formula $[MgCO_3\cdot 3H_2O]$, as the bicarbonate-derived band at 985 cm^{-1} (Zhang et al., 2006) was not present (Fig. 1). Scanning electron microscopy (SEM) (Fig. 3) revealed a needle-like morphology typical of nesquehonite (*c.f.*, Harrison et al., 2013a, 2017; Power et al., 2009; Schaef et al., 2011; Zhao et al., 2010). Neither XRD nor FTIR data revealed significant differences between the two batches of synthetic nesquehonite (Figs. 1 and 2), though SEM revealed a slightly higher proportion of fine particles in the second synthesized batch, which was used for the longer-term experiments.

2.2. Experimental methods

Experiments to determine the solubility product of nesquehonite were conducted at constant temperatures of 5 °C, 25 °C, and 35 °C. A single experiment was conducted at 5 °C, whereas duplicate experiments were conducted at 25 °C and 35 °C. The duplicate experiments ran subsequently to the originals, and for a longer duration, to ensure the complete conversion of nesquehonite to dypingite. Each experiment consisted of a suite of nine to eleven sealed, closed-system reactors. The starting aqueous solution and solid were first added to the individual reactors (Nalgene bottles) in identical amounts. Each bottle contained 0.60 g of nesquehonite and ~73 g of an aqueous solution containing 0.10 mol/L NaCl and 0.06 mol/L $NaHCO_3$. At various selected times, an individual reactor was sampled in its entirety (liquid and solid). This approach was taken to ensure the solid and its contemporaneous fluid were collected, and to avoid generation of headspace due to sampling, as would occur by sampling fluids from a single reactor. The individual reactors were filled with minimal headspace to inhibit loss of $CO_{2(g)}$ from solution. To avoid precipitation due to temperature changes, the experimental solutions were prepared by first heating or cooling distilled, de-ionized water (18.2 MΩ cm) to the desired experimental temperature, followed by the addition of reagent-grade NaCl and $NaHCO_3$ to reach the desired concentration. This aqueous solution was then poured into the individual reactors, which already contained nesquehonite, and the reactors were rapidly sealed, weighed, and placed at the experimental temperature. Experiments conducted at 5 °C were placed on an orbital shaker in a thermostatic refrigerator, whereas experiments conducted at 25 °C and 35 °C were placed in shaking water baths at constant temperature.

Individual reactors were sampled one at a time to track the chemical composition of the reactive aqueous solution, as well as changes in the mineral composition of the solids. Upon sampling, reactors were weighed to assess evaporative losses and the solution temperature was measured using a thermometer. The solution was then removed via a syringe and needle, and filtered with a 0.22 µm polyethersulfone (PES) syringe filter. Two aliquots were immediately acidified to 2% HNO_3 for subsequent analysis of Mg concentrations, and a single aliquot was used for immediate pH measurements, and later alkalinity measurements. Fluid pH was measured using a Metrohm 913 pH-meter and a Metrohm combined electrode (6.0234.1000) that was calibrated using NIST traceable pH 25 °C 4.01, 7.00, and 9.18 buffer solutions at each experimental temperature, with an uncertainty of approximately ± 0.03 pH units. Dissolved inorganic carbon concentration was calculated using PHREEQC V3 (Parkhurst and Appelo, 2013) and a modified LLNL database, based on the measured fluid compositions. Geochemical modeling methods are discussed in further detail in Section 2.4.

The solids were separated from any remaining solution via vacuum filtration, and were rinsed with distilled, de-ionized water to prevent NaCl precipitation. They were then dried at room temperature for ~48 h and stored in a desiccator prior to analysis. Note that hydrated

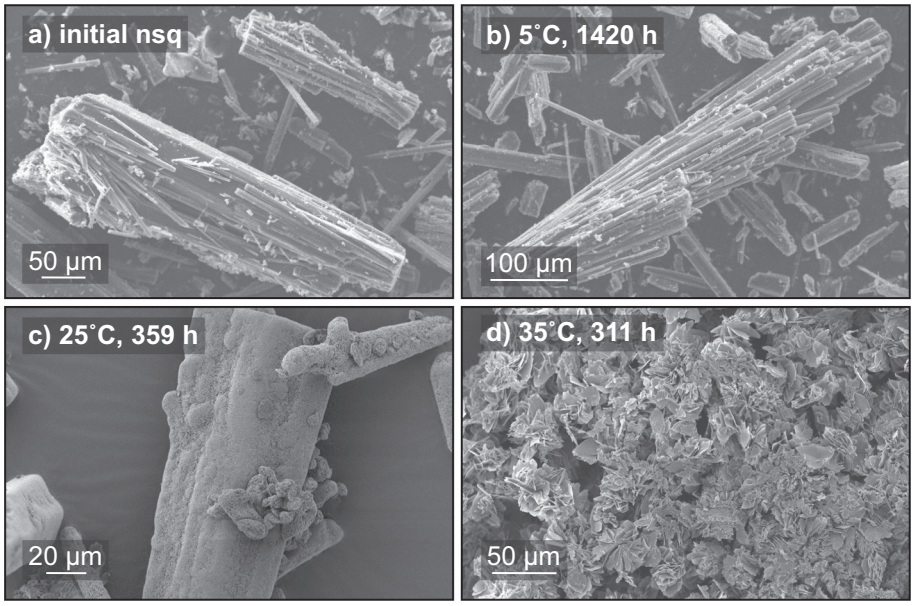

Fig. 3. Scanning electron micrographs of solids. A) Initial nesquehonite. B) Solid sample after 1420 h at 5 °C. C) Solid sample after 359 h at 25 °C. D) Solid sample after 311 h at 35 °C.

Mg-carbonate minerals must be stored under dry conditions to prevent their transformation to other Mg-carbonate minerals in humid air (Davies and Bubela, 1973; Power et al., 2016), therefore care was taken to minimize exposure to laboratory air at all times.

Dypingite was formed in situ within the reactors at 25 °C and 35 °C, with longer-term experiments designed to allow the complete transformation from nesquehonite to dypingite and to capture a period of stable solution chemistry representative of equilibrium between the dypingite and the reactive aqueous solution. The phase transformation was tracked via changes in aqueous solution composition and mineralogical data collected using XRD complemented with FTIR for some samples.

2.3. Analytical techniques

The alkalinity of all fluid samples was determined by HCl titration using an automated Schott Titroline Alpha Plus titrator. Long term reproducibility, determined from repeated analysis of a standard, was better than $\pm 0.36 \times 10^{-2}$ mol/L (3σ), and the detection limit was 5×10^{-5} mol/L. Dissolved inorganic carbon (DIC) concentrations were calculated using the measured fluid composition and PHREEQC V3 (Parkhurst and Appelo, 2013) with a modified LLNL database, as described in further detail in Section 2.4. The uncertainty introduced via the calculation of DIC is unknown; a minimum uncertainty equal to that of the alkalinity measurement is assumed ($\pm 0.36 \times 10^{-2}$ mol/L). Aqueous Mg concentrations were measured by atomic absorption spectroscopy (AAS) using a Perkin Elmer AAnalyst 400. Samples and standards were matrix-matched in 0.01 mol/L HNO_3. All samples were measured in triplicate and reported concentrations represent averages of these measurements, the standard deviation (3σ) is smaller than the symbols employed in figures, unless otherwise shown. Reproducibility was better than 2%, and the quantification and detection limits were 9.6×10^{-8} mol/L and 2.9×10^{-8} mol/L, respectively. Quantification and detection limits were defined as 10σ and 3σ over background variation.

The mineralogical compositions of the solids were determined using powder XRD with a Bruker D2 Phaser with Cu radiation. The scan speed was 0.5 s/step, and a step size of 0.02°/step was used. To complement XRD data, FTIR analysis was conducted on select samples using a ThermoScientific Nicolet iN 10 MX infrared imaging microscope. Morphological characteristics were examined via scanning electron microscopy using a JEOL JSM 6360LV or a JEOL JSM 6480LV.

2.4. Geochemical modeling

The standard state adopted in this study is that of unit activity at any temperature and pressure for pure minerals. The standard state for aqueous species at any temperature and pressure is unit activity of a hypothetical 1 m solution referenced to infinite dilution. Aqueous speciation and mineral saturation states were calculated using PHREEQC V3 (Parkhurst and Appelo, 2013) and its LLNL database, which was modified to include the carbonic acid dissociation constants of Patterson et al. (1982, 1984), the hydrolysis constant for Mg^{2+} from Palmer and Wesolowski (1997), the formation constants of $MgHCO_3^+$ and $MgCO_3^\circ$ ion pairs from Stefansson et al. (2014), the magnesite solubility product from Bénézeth et al. (2011), the hydromagnesite solubility product from Gautier et al. (2014), and the brucite solubility product from Brown et al. (1996). Activity coefficients are calculated using the b-dot model (Helgeson, 1969).

3. Results

3.1. Phase transformations

3.1.1. Phase transformation at 25 °C

The measured Mg concentration, pH, alkalinity, mineralogical composition, and the calculated DIC concentration and aqueous Mg^{2+}, CO_3^{2-}, and H_2O activities with time in all experiments are listed in Table 1. At 5 °C, nesquehonite did not transform into a different phase throughout the 1420 h (59 d) experiment as confirmed by XRD (Electronic Supplement (ES)-Fig. 1). Similarly, SEM micrographs revealed that the solid phase maintained the needle-like nesquehonite morphology throughout the experiment (Fig. 3).

At 25 °C, minor dypingite was first detected with XRD at 359 h in the long-term experiment, and dypingite formed between 367 h and 1086 h during the short-term experiment (ES-Figs. 2 and 3). Trace dypingite was also detected in the 22 h sample in the long-term 25 °C experiment. However, the solution composition did not change, dypingite was not present in the 122 h sample, nor was it present over this timeframe in the short-term 25 °C experiment. Together, this suggests that its presence in the 22 h sample from the long-term experiment is an artifact of improper sample storage, not dypingite formation in the experiment.

Table 1
Aqueous composition, aqueous activities, and mineralogical composition measured over time for all experiments.

Experiment	Time (h)[a]	pH (± 0.03)	Alkalinity (× 10^{-2} mol/L; ± 0.36 × 10^{-2})	DIC[b] (× 10^{-2} mol/L; ± 0.36× 10^{-2})	Mg (× 10^{-2} mol/L)	Mg error (3σ × 10^{-2})	a_{Mg2+}[c] (× 10^{-3})	a_{CO32-}[c] (× 10^{-3})	a_{H2O}[c]	Mineralogy[d]
5	0	8.25	5.95	6.00				0.19	0.995	nsq
	6	9.44	9.04	7.54	1.214	0.005	2.431	2.88	0.994	nsq
	9	9.40	8.90	7.54	1.157	0.004	2.381	2.65	0.994	nsq
	12	9.41	8.94	7.49	1.290	0.012	2.641	2.71	0.994	nsq
	24	9.39	9.17	7.75	1.269	0.010	2.586	2.70	0.994	nsq
	49	9.43	9.16	7.65	1.278	0.017	2.558	2.87	0.994	nsq
	120 (nsq)	9.47	9.66	7.91	1.510	0.006	2.915	3.15	0.994	nsq
	367 (nsq)	9.59	9.71	7.66	1.505	0.006	2.734	3.76	0.994	nsq
	1085 (nsq)	9.39	9.68	8.14	1.498	0.016	3.001	2.78	0.994	nsq
	1420 (nsq)	9.59	9.67	7.62	1.502	0.014	2.732	3.75	0.994	nsq
25_short	0	8.15	5.94	5.97				0.25	0.995	nsq
	4	9.20	8.99	7.52	1.167	0.015	1.976	2.85	0.994	nsq
	6	9.20	8.99	7.55	1.094	0.011	1.847	2.86	0.994	nsq
	8	9.19	8.87	7.47	1.119	0.003	1.926	2.75	0.994	nsq
	10	9.18	8.61	7.27	1.075	0.019	1.882	2.67	0.994	nsq
	12	9.20	8.72	7.31	1.114	0.008	1.920	2.76	0.994	nsq
	24 (nsq)	9.19	8.95	7.50	1.197	0.013	2.048	2.79	0.994	nsq
	49 (nsq)	9.19	8.97	7.52	1.183	0.002	2.022	2.79	0.994	nsq
	120 (nsq)	9.20	9.02	7.54	1.192	0.011	2.019	2.85	0.994	nsq
	367 (nsq)	9.19	9.05	7.59	1.216	0.015	2.076	2.79	0.994	nsq
	1086	8.97	8.99	8.00	1.113	0.006	2.158	1.95	0.994	nsq + dyp
25_long	0	8.23	5.92	5.92	0.0006	0.0001	0.002	0.30	0.995	nsq
	22 (nsq)	9.27	8.68	7.12	1.105	0.011	1.821	3.08	0.994	nsq (minor dyp)
	122 (nsq)	9.23	8.69	7.23	1.098	0.009	1.861	2.88	0.994	nsq
	359	8.94	8.69	7.77	1.119	0.012	2.249	1.78	0.994	nsq + dyp
	599	8.82	8.66	7.95	1.075	0.001	2.296	1.42	0.994	nsq + dyp
	843	8.88	8.69	7.87	1.104	0.007	2.288	1.59	0.994	nsq + dyp
	987	8.86	8.09	7.38	1.011	0.020	2.187	1.43	0.994	nsq + dyp
	1157	8.82	8.49	7.80	1.065	0.012	2.303	1.38	0.994	dyp + nsq
	1367 (dyp)	8.81	8.49	7.81	1.069	0.010	2.325	1.35	0.994	dyp + dyp-like
	1607 (dyp)	8.81	8.61	7.93	1.051	0.062	2.265	1.38	0.994	dyp + dyp-like
	2043 (dyp)	8.90	8.49	7.68	1.036	0.008	2.148	1.62	0.994	dyp + dyp-like
35_short	0	8.11	5.94	5.96	0.0004	nd[e]	0.001	0.28	0.995	nsq
	3 (nsq)	9.12	8.77	7.35	1.051	0.008	1.629	2.82	0.994	nsq
	5 (nsq)	9.12	8.64	7.24	1.063	0.018	1.670	2.75	0.994	nsq
	7 (nsq)	9.14	8.63	7.21	1.047	0.015	1.625	2.83	0.994	nsq
	11 (nsq)	9.11	8.65	7.27	1.050	0.016	1.654	2.73	0.994	nsq
	24 (nsq)	9.22	8.74	7.11	1.048	0.010	1.519	3.26	0.994	nsq
	75	9.19	8.75	7.18	1.062	0.004	1.573	3.12	0.994	nsq (trace dyp)
	122	9.12	8.74	7.33	1.054	0.007	1.647	2.78	0.994	nsq + dyp
	191	9.04	8.78	7.52	1.080	0.008	1.778	2.45	0.994	nsq + dyp
	243	9.02	8.65	7.46	1.048	0.011	1.767	2.32	0.994	nsq + dyp
	432	8.84	8.43	7.61	0.900	0.004	1.705	1.70	0.994	dyp + nsq
35_long	0	8.08	5.93	5.96	0.001	0.0001	0.004	0.26	0.995	nsq
	26 (nsq)	9.17	8.54	7.06	1.044	0.002	1.596	2.93	0.994	nsq
	74 (nsq)	9.20	8.57	7.02	1.056	0.009	1.577	3.08	0.994	nsq
	123	9.09	8.60	7.26	1.057	0.015	1.697	2.62	0.994	nsq (trace dyp)
	244	8.90	8.66	7.66	1.138	0.011	2.082	1.88	0.994	nsq + dyp
	311	8.80	8.14	7.37	1.048	0.002	2.087	1.49	0.994	dyp + nsq
	482 (dyp)	8.65	8.36	7.80	0.951	0.007	2.018	1.15	0.994	dyp
	552 (dyp)	8.64	7.58	7.09	0.922	0.009	2.057	1.02	0.994	dyp
	600 (dyp)	8.63	8.29	7.77	0.930	0.007	1.999	1.10	0.994	dyp
	718	8.63	8.18	7.67	0.915	0.007	1.977	1.09	0.994	dyp + unknown phase
	932 (dyp)	8.65	8.18	7.65	0.885	0.007	1.892	1.14	0.994	dyp
	1368 (dyp)	8.72	8.12	7.51	0.849	0.007	1.758	1.29	0.994	dyp

[a] (nsq) indicates time points used for the calculation of K_{sp}^{nsq}, and (dyp) indicates timepoints used for the calculation of K_{sp}^{dyp}.
[b] DIC = dissolved inorganic carbon; calculated using PHREEQC V3.
[c] Aqueous activity calculated using PHREEQC V3.
[d] determined with X-ray diffraction.
[e] No data.

The sample collected at 359 h in the long-term experiment exhibits particles with needle-like external morphology, similar to the initial nesquehonite, but with rounded edges, and a flakey, porous surface (Fig. 3c). This flakey morphology is typical of dypingite (e.g., Canterford et al., 1984; Mavromatis et al., 2012; Power et al., 2007), and suggests the precipitation of dypingite is closely coupled to the dissolution of nesquehonite at the mineral-fluid interface, as has been observed for several mineral replacement reactions (e.g., Ruiz-Agudo et al., 2012 and references therein). Within 1367 h, nesquehonite was completely replaced by dypingite, which remained until the end of the 2043 h (85 d) long-term experiment (ES-Fig. 3). Dypingite is normally reported in the literature to have the chemical formula $[Mg_5(CO_3)_4(OH)_2{\cdot}5H_2O]$, but has also been reported to have the formula $[Mg_5(CO_3)_4(OH)_2{\cdot}8H_2O]$, and more rarely $[Mg_5(CO_3)_4(OH)_2{\cdot}6H_2O]$ (Canterford et al., 1984; Hopkinson et al., 2012; Kristova et al., 2014; Raade, 1970; Xiong and Lord, 2008). The

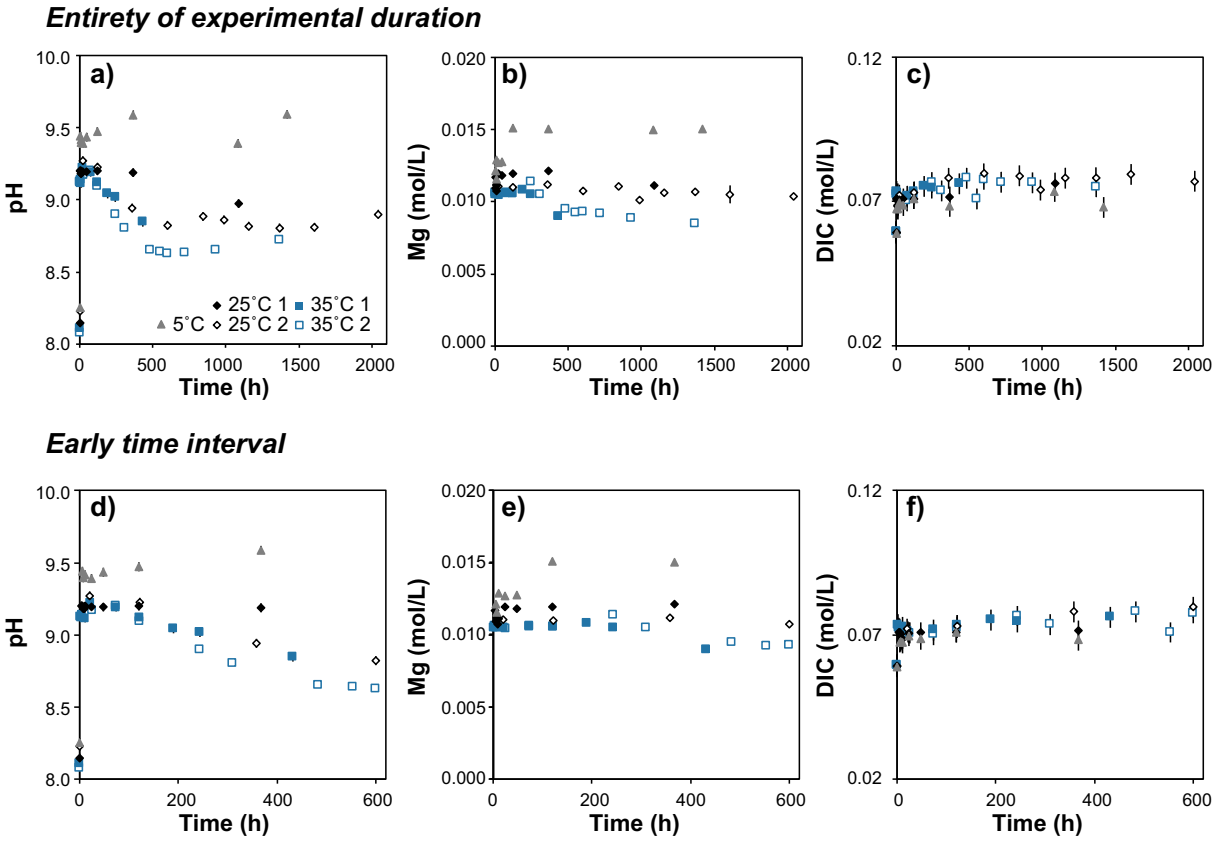

Fig. 4. Fluid composition over time in all experiments. Fluid composition evolution for the entire experimental duration: A) pH, B) Mg concentration, C) dissolved inorganic carbon concentration (DIC). Fluid composition evolution for the first 600 h of each experiment: D) pH, E) Mg concentration, F) DIC. Data from the 5 °C, 25 °C, and 35 °C experiments are indicated by gray triangles, black diamonds, and blue squares, respectively, and short- and long-term experiments are indicated by filled and open points, respectively. Error is smaller than symbols unless otherwise shown. (For interpretation of the references to colour in this figure legend, the reader is referred to the web version of this article.)

XRD pattern of the dypingite in our experiments was consistent with $[Mg_5(CO_3)_4(OH)_2{\cdot}8H_2O]$ (International center for diffraction data, pattern PDF-00-029-0857; ES-Figs. 3–5), which differs from that of $[Mg_5(CO_3)_4(OH)_2{\cdot}5H_2O]$ (International center for diffraction data, pattern PDF-00-023-1218), by the presence of a low angle peak at 2.659° 2θ (d = 33.200). Other than this peak, the similarity of the XRD patterns for dypingite with 5 or 8 hydration waters means the presence of $[Mg_5(CO_3)_4(OH)_2{\cdot}5H_2O]$ in addition to $[Mg_5(CO_3)_4(OH)_2{\cdot}8H_2O]$ cannot be excluded.

An additional phase was observed in the long-term experiment from 599 h until the end of the experiment; this additional phase is characterized by two small, low-angle peaks (labeled "d-1" in ES-Fig. 3). Dypingite-like phases with varying degrees of hydration and similar structures, which exhibit low-angle XRD peaks, have been observed in several studies (Ballirano et al., 2013; Davies and Bubela, 1973; Hopkinson et al., 2008, 2012; Kristova et al., 2014). For example, during the degassing of a Mg-CO_3 solution at 58 °C, Hopkinson et al. (2012) observed what they referred to as several "dypingite-type" phases with similar crystal structures but different cell volumes and varying numbers of waters of hydration, including $[Mg_5(CO_3)_4(OH)_2{\cdot}8H_2O]$. Additional peaks not reported in the established dypingite XRD patterns were also observed at ~3.5° and ~6° by Ballirano et al. (2013) during the phase transformation of nesquehonite at room temperature. These low angle peaks and their inconsistent appearance are attributed to the large and varied cell-volume of dypingite-like phases, different stacking-sequences of the layers of MgO_6 and carbonate groups, or different water contents (Ballirano et al., 2013). As such, the low angle peaks observed from 599 h until the end of the experiment, are attributed to an additional dypingite-like phase, potentially differing in cell volume and/or number of hydration waters. To further evaluate the dypingite-like phase documented at 25 °C, the FTIR spectrum of a sample containing this phase (25 °C, 1607 h) was compared to the FTIR spectrum of a sample from the long-term 35 °C experiment, which contained only XRD-identifiable dypingite (35 °C, 560 h). The FTIR spectra are close to identical (Fig. 1), consistent with the interpretation that the unnamed phase documented in the 25 °C experiments is likely another dypingite-like phase.

Changes in fluid composition were coincident with the phase transformation documented with XRD. During the phase transformation, pH decreased from ~9.2 to ~8.8 between 120 h and 599 h before stabilizing at ~8.8 for the remainder of the experiment (Fig. 4a and d). This suggests that the phase transformation consumes protons despite forming a hydroxyl-bearing phase. The Mg concentration exhibited a minor decrease during the phase transformation (Fig. 4b and e), whereas the DIC exhibited a slight increase (Fig. 4c and f). After 599 h, DIC and Mg concentration again remained stable for the remainder of the experiment (Fig. 4b and c).

3.1.2. Phase transformation at 35 °C

At 35 °C, the transformation from nesquehonite to dypingite was more rapid than at 25 °C. Dypingite was first detected at trace levels by XRD in the 75 h sample from the short-term experiment (ES-Fig. 4), and in the 123 h sample from the long-term experiment (ES-Fig. 5). Similar to the 25 °C experiment, the dypingite XRD pattern was consistent with that of $[Mg_5(CO_3)_4(OH)_2{\cdot}8H_2O]$ (International center for diffraction data, pattern PDF-00-029-0857; ES-Figs. 4 and 5). The additional dypingite-like phase observed at 25 °C was not evident in the 35 °C experiments, however, a different unidentified phase was recorded in the sample at 718 h in the long-term experiment (identified as "unknown"

in ES-Fig. 5), evidenced by additional peaks at ~27° and ~33° and the disappearance of the ~11° peak. It is not clear whether this was an additional phase, or representative of a change in the dypingite structure. This phase was not present before or after 718 h, nor was it detected in the short-term experiment. It may be an artifact of imperfect sample storage, rather than reflecting an in situ mineralogical change in the reactors. However, if there were a mineral phase change within the reactor, that would impact solubility calculations. Thus, this sample was not included in calculation of the solubility product. Nesquehonite was no longer present within 482 h at 35 °C (ES-Fig. 5), compared to 1367 h for complete conversion of nesquehonite at 25 °C.

SEM images revealed a different evolution of crystal morphology between the 25 °C and 35 °C experiments; unlike at 25 °C, the external crystal morphology of nesquehonite was not maintained. Rather, over a similar time-frame, the needle-like morphology was replaced by flakey aggregates with typical dypingite morphology (Fig. 3d) (e.g., Canterford et al., 1984; Mavromatis et al., 2012; Power et al., 2007). This difference in morphological evolution may be a consequence of the different reaction rates. In both cases, the morphology change suggests the mineral phase transformation occurs via dissolution-reprecipitation. However, the slower rate of nesquehonite dissolution at 25 °C coupled to the rapid re-precipitation as dypingite could result in the observed pseudo-morphic replacement at this temperature. Conversely, a relatively high nesquehonite dissolution rate compared to dypingite precipitation rate at 35 °C, would allow a spatial and thus morphological separation of the two phases.

Similar to the fluid composition change observed during the phase transformation at 25 °C, the pH, Mg concentration, and DIC concentration evolved during the nesquehonite-dypingite transformation at 35 °C (Fig. 4). A decrease in pH from ~9.15 to ~8.66 occurred between ~74 h and 482 h (Fig. 4a and d), while a slight decline in Mg concentration was observed after 310 h (Fig. 4b and e). The decline in Mg concentration occurred when the solids became dominated by dypingite, rather than by nesquehonite (Table 1). A slight decrease in Mg concentration continued for the remainder of the 35 °C experiment, suggesting either a slow approach to dypingite equilibrium, or perhaps the beginning of a transformation to a less hydrated Mg-carbonate, though no further mineralogical changes were detected with XRD or FTIR. A minor increase in DIC concentration was observed after 75 h (Fig. 4c and f), but DIC was again fairly constant from ~243 h to the end of the short- and long-term experiments. The short-term experiments were too brief for completion of the nesquehonite-dypingite transformation, but the trends in fluid composition were consistent with the early stages of the transformation documented in the longer-term experiments.

3.2. Retrieval of the nesquehonite solubility product

The dissolution of nesquehonite to a constant fluid composition was rapid in all experiments, with pH, Mg, and alkalinity increasing to constant values within 120 h, 24 h, and 3 h in the 5 °C, 25 °C, and 35 °C experiments, respectively (Table 1; Fig. 4). The values used for the calculation of nesquehonite and dypingite solubility products at all temperatures are indicated in Table 1. Brucite [$Mg(OH)_2$], which can form at room temperature from Mg-rich solutions, remained undersaturated in all experiments. Nesquehonite was the only phase detected with XRD throughout the 5 °C experiment (ES-Fig. 1), therefore all samples taken from 120 h, when the fluid composition stabilized, up to the end of the experiment (1420 h) were included in the calculation of its solubility product (K_{sp}^{nsq}). In the 25 °C experiment, nesquehonite was the only phase detectable with XRD for 367 h in the short-term experiment (ES-Fig. 2), though minor dypingite was detected at 359 h in the long-term experiment (ES-Fig. 3). Solution compositions remained relatively constant over these time periods, therefore samples from between 24 h and 367 h in the short-term experiment, and less than 359 h in the long-term experiment were used for the calculation of $K_{sp,\,25}^{nsq}$, providing a total of six distinct points for which the solubility product was calculated and averaged.

In the 35 °C experiment, the solubility product was calculated using the aqueous solution composition between 3 h and 24 h in the short-term experiment, and 26 h and 74 h in the long-term experiment (seven time points in total), representing time points that had constant fluid composition and no detectable dypingite (Table 1).

The nesquehonite solubility product was determined using the average of the calculated Mg^{2+} and CO_3^{2-} aqueous activities according to the reaction

$$MgCO_3{\cdot}3H_2O \leftrightharpoons Mg^{2+} + CO_3^{2-} + 3H_2O \quad (1)$$

and its law of mass action

$$K_{sp}^{nsq} = a_{Mg^{2+}}\, a_{CO_3^{2-}}\, a_{H_2O}{}^3 \quad (2)$$

The aqueous activities in Eq. (2) were calculated using PHREEQC V3 with the modified LLNL database, as described in Section 2.4, and are listed in Table 1. The nesquehonite solubility products are reported in Table 2.

Based on the solubility product determined in this study, the standard molar Gibbs free energy of formation of nesquehonite was also calculated. The standard state properties of the aqueous species involved in Eq. (1) were used, and are listed in Table 3. The enthalpy of the nesquehonite dissolution reaction (Eq. (1)) was estimated by plotting the natural logarithm of the solubility product versus reciprocal temperature (Fig. 5, as shown with base 10 logarithm), with the slope of the line equated to $-\Delta H_r^{\circ}/R$, where ΔH_r° is the enthalpy of reaction, and R is the ideal gas constant (Table 3). The standard enthalpy of formation of nesquehonite was then calculated using the standard state properties of the aqueous species involved in Eq. (1), as listed in Table 3.

3.3. Retrieval of the dypingite solubility product

The solubility product of dypingite (K_{sp}^{dyp}) was estimated from the long-term 25 °C and 35 °C experiments in which complete transformation to dypingite was achieved. Dypingite was not formed at 5 °C, likely due to slower kinetics of the transformation reaction, thus its solubility product was not determined at this temperature. At 25 °C, nesquehonite was no longer detected after 1367 h (Table 1; ES-Fig. 3), and the fluid composition was relatively constant for the remainder of the experiment. This period is therefore taken to reflect equilibrium between dypingite and the aqueous solution, and the solubility product was calculated from the final three samples from this experiment (Table 1). At 35 °C, nesquehonite was no longer detected after 482 h (Table 1; ES-Fig. 5); the fluid composition also remained relatively constant for the remainder of the experiment. The fluid composition from 482 h until the end of the experiment was therefore used to calculate K_{sp}^{dyp} (Table 1), except for the sample taken at 718 h, due to the presence of an unidentified phase in the solid sample as previously described. A total of five distinct points were used for the solubility product calculation at 35 °C. Aqueous activities of Mg^{2+} and CO_3^{2-} were calculated using PHREEQC V3 and the modified LLNL database, and OH^- activity was calculated from pH measurements. The K_{sp}^{dyp} was calculated using these values and Eqs. (3) and (4).

$$Mg_5(CO_3)_4(OH)_2{\cdot}{\sim}nH_2O \leftrightharpoons 5Mg^{2+} + 4CO_3^{2-} + 2OH^- + nH_2O \quad (3)$$

$$K_{sp}^{dyp} = a_{Mg^{2+}}{}^5\, a_{CO_3^{2-}}{}^4 a_{OH^-}{}^2\, a_{H_2O}{}^n \quad (4)$$

where the variable, n, was 5 or 8. The presence of at least two dypingite-like phases in the 25 °C experiments, and potentially both [$Mg_5(CO_3)_4(OH)_2{\cdot}5H_2O$] and [$Mg_5(CO_3)_4(OH)_2{\cdot}8H_2O$] in the 35 °C experiments means that the value calculated for the dypingite solubility product likely represents a mixture of dypingite-like phases of varying degrees of hydration. Due to the uncertainty in the exact hydration state of dypingite, and the presence of an additional dypingite-like phase at 25 °C, the K_{sp}^{dyp} was calculated in three ways. Either the activity of water was assumed to be unity, or the activity of water was calculated

Table 2
Solubility products for nesquehonite and dypingite from this study and previous works including the PHREEQC databases.

Temperature (°C)	Nesquehonite logK_{sp}^{nsq}							Dypingite logK_{sp}^{dyp}		
	This study ± 3σ	PHREEQC		Wang and Li (2012)	Kline (1929)	Langmuir (1965)	Hostetler (1964)	This study		
		Minteqv4	LLNL					a_{H_2O} = 1 ± 3σ	$8H_2O$ ± 3σ	$5H_2O$ ± 3σ
5	−5.03 ± 0.13	−4.36	−4.53	−4.99						
25	−5.27 ± 0.15	−4.67	−5.06	−5.27	−4.96	−5.59 ± 0.1 or −5.42[a]	−5.51	−34.93 ± 0.58	−34.95 ± 0.58	−34.94 ± 0.58
35	−5.34 ± 0.04	−4.81	−5.23	−5.40				−36.02 ± 0.31	−36.04 ± 0.31	−36.03 ± 0.31

[a] considering the $MgHCO_3^+$ and/or $MgCO_3^\circ$ aqueous complexes (reported by Robie and Hemingway (1973) based on the data of Langmuir (1965).

based on the solution composition using PHREEQC V3, and K_{sp}^{dyp} was determined using eight or five waters of hydration and Eq. (4). These are the most commonly reported stoichiometries for dypingite and have XRD patterns that are consistent with our experimental data. The K_{sp}^{dyp} values calculated in each case were equivalent within error (Table 2), demonstrating that uncertainty in the hydration state of dypingite does not strongly affect the K_{sp}^{dyp} retrieved at the experimental ionic strength. The solubility product (Table 2) decreased slightly with increasing temperature, consistent with the behavior of nesquehonite (this study) and hydromagnesite [$Mg_5(CO_3)_4(OH)_2{\cdot}4H_2O$] (Gautier et al., 2014).

4. Discussion

4.1. Nesquehonite and dypingite solubility products

The standard molar Gibbs free energy of formation of nesquehonite calculated from our data was in very good agreement with that determined by Robie and Hemingway (1973), and Langmuir (1965), and the standard molar enthalpy of formation calculated from our data was in very good agreement with Robie and Hemingway (1973) (Table 3). The nesquehonite solubility product calculated from our data decreases slightly with increasing temperature, consistent with the solubility of other Mg- and Ca-carbonate minerals (Table 2) (e.g., Bénézeth et al., 2011, 2018; Gautier et al., 2014; Königsberger et al., 1999; Marion, 2001), and temperature dependence reported for nesquehonite solubility in previous studies (Dong et al., 2008; Wang and Li, 2012).

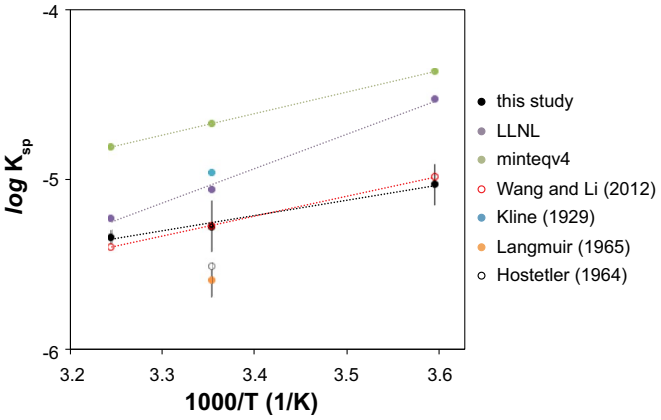

Fig. 5. Logarithm of nesquehonite solubility products (K_{sp}^{nsq}) versus reciprocal of temperature (in Kelvin).

Table 3
Standard state properties (25 °C, 1 bar) of nesquehonite reported in the literature and determined in this study, and standard state properties of dypingite determined in this study. The standard state properties of aqueous species used to calculate the Gibbs free energy of formation of nesquehonite and dypingite in the present study are reported in the lower table, as are the equilibrium constants of the considered aqueous Mg complexes at 25 °C.

Source	ΔG_r° (kJ/mol)	ΔG_f° (kJ/mol)	ΔH_r° (kJ/mol)	ΔH_f° (kJ/mol)
		Nesquehonite [$MgCO_3 \cdot 3H_2O$]		
This study	30.1 ± 0.8	−1723.5 ± 0.8	−17.17	−1981.5
Robie and Hemingway (1973)		−1724.0 ± 0.5		−1977.3 ± 0.5
Langmuir (1965)		−1726.6 ± 2.1		
		Dypingite [$Mg_5(CO_3)_4(OH)_2 \cdot 8H_2O$]		
This study	199.5 ± 1.3	−6792.8 ± 1.3		

Aqueous species

Source	Species	ΔG_f° (kJ/mol)	S (J/mol/K)	ΔH_f° (kJ/mol)
Wagman et al. (1982)	H_2O	−237.13	69.95	−285.83
Shock and Helgeson (1988), Shock et al. (1997)	Mg^{2+}	−453.98	−138.07	−465.96
Shock and Helgeson (1988)	CO_3^{2-}	−527.98	−50.00	−675.24
Wagman et al. (1982)	HCO_3^-	−586.77	91.20	−691.99
Wagman et al. (1982)	OH^-	−157.24	−10.75	−229.99

Aqueous complexes

Source	Species	log$K$	Reaction
Stefansson et al. (2014)	$MgHCO_3^+$	1.1	$Mg^{2+} + HCO_3^- \leftrightharpoons MgHCO_3^+$
Stefansson et al. (2014)	$MgCO_3^\circ$	3.0	$Mg^{2+} + CO_3^{2-} \leftrightharpoons MgCO_3^\circ$
Palmer and Wesolowski (1997)	$Mg(OH)^+$	−11.7	$Mg^{2+} + H_2O \leftrightharpoons MgOH^+ + H^+$
PHREEQC V3 LLNL database	$MgCl^+$	−0.1	$Mg^{2+} + Cl^- \leftrightharpoons MgCl^+$

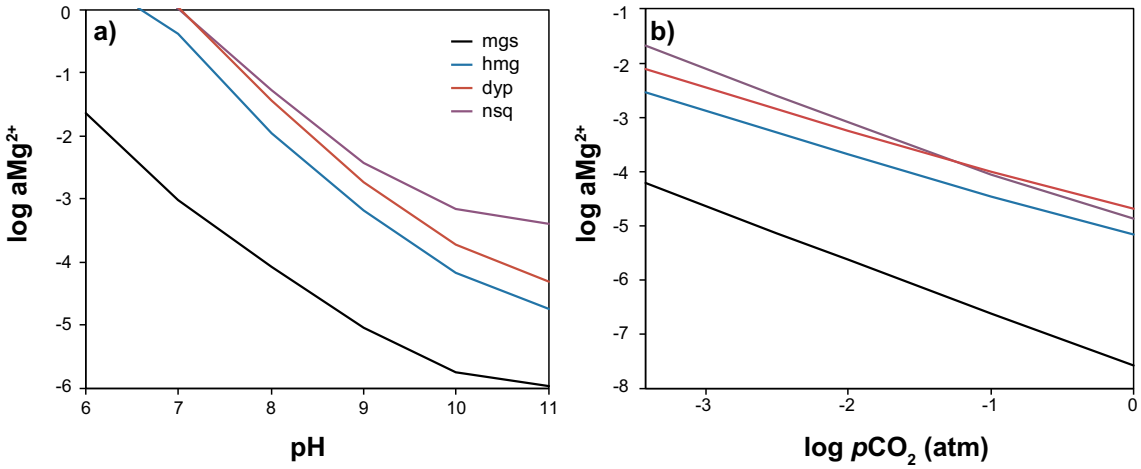

Fig. 6. Relative stability of hydrated Mg-carbonates at 25 °C. A) Mg^{2+} activity in equilibrium with magnesite, hydromagnesite, dypingite, and nesquehonite as a function of pH. The total dissolved inorganic carbon concentration was fixed at 0.06 M, the Na concentration was fixed at 0.16 M, and the Cl concentration was fixed at 0.10 M to reflect the conditions in the experiments. B) Mg^{2+} activity in equilibrium with magnesite, hydromagnesite, dypingite, and nesquehonite as a function of pCO_2. The pH was fixed at 9, Na concentration was fixed at 0.16 M, and Cl concentration fixed at 0.10 M to reflect the conditions in the experiments. Calculations were done using PHREEQC V3 and the modified LLNL database, as described in Section 2.4.

However, the temperature dependence is not significant outside 3σ uncertainty (Table 2; Fig. 5). Our values are in good agreement with those reported in the modeling study of Wang and Li (2012), which considered the impact of aqueous speciation on nesquehonite solubility in saline solutions (Table 2). However, discrepancies are evident between our values and some of the corresponding values at 25 °C reported in the literature; values in the present study fall between those of Kline (1929), Langmuir (1965), and Hostetler (1964) (Table 2; Fig. 5); such differences could be attributed to differences in the calculation of aqueous speciation. The $\log K_{sp}^{nsq}$ in both the LLNL and minteqv4 PHREEQC databases are most similar to that of Kline (1929), and are considerably larger than those measured in this study as well as the values reported by Langmuir (1965) and Hostetler (1964) (Table 2; Fig. 5). In addition, the temperature extrapolation employed in both of these databases exhibits a stronger temperature dependence than that measured in the present study, or that indicated by Wang and Li (2012) (Fig. 5). The neglect of aqueous speciation in the calculation of the solubility product of Kline (1929) likely explains the discrepancy between this value and that calculated in our study, as also suggested by Langmuir (1965) to explain differences between reported nesquehonite solubility products. The reason for the discrepancy between our measured values and those reported by Hostetler (1964) and Langmuir (1965) is less clear, but may again relate to differences in the treatment of aqueous speciation. Robie and Hemingway (1973) suggest that the calorimetric data from their study are only in agreement with the solubility data of Langmuir (1965) if the aqueous complexation assumed by Langmuir (1965) is overestimated. This could also account for the discrepancy between the Langmuir (1965) value and that calculated here. As, the present study used recent data for the complexation of aqueous Mg-carbonate species (Stefansson et al., 2014), which were not available at the time of the Hostetler (1964) and Langmuir (1965) studies and much of the data regarding aqueous Mg-carbonate complex stability came after these studies (Stefansson et al., 2014 and references therein). In addition, the reported stability of $MgCO_3^\circ$ and $MgHCO_3^+$ aqueous complexes at 25 °C reported in early literature was highly variable (Stefansson et al., 2014). It is therefore unsurprising that solubility products determined for magnesium carbonates like nesquehonite differ between studies that used different thermodynamic data for aqueous speciation. The similarity between the Kline (1929) value and those used in the LLNL and minteqv4 databases suggests they may also lack consideration of aqueous complexation, thus we propose that values reported in the present study and by Wang and Li (2012) are more appropriate for calculating nesquehonite saturation state.

The dypingite solubility product has not previously been reported, therefore our calculated K_{sp}^{dyp} cannot be compared with other dypingite values. Instead, we compare our K_{sp}^{dyp} values to those of hydromagnesite, a structurally similar but less hydrated Mg-carbonate. Our calculated K_{sp}^{dyp} is higher than those reported for hydromagnesite at 25 °C: $K_{sp,\ 25}^{hmg} = 10^{-37.08}$ (Gautier et al., 2014), and $10^{-41.56}$ (Xiong, 2011), compared to $K_{sp,\ 25}^{dyp,\ 8H2O} = 10^{-34.95 \pm 0.58}$. This is consistent with previous observations of dypingite behavior, as it is commonly observed to transform to hydromagnesite over time (Ballirano et al., 2013; Davies and Bubela, 1973; Hopkinson et al., 2008, 2012; Sutradhar et al., 2011), reflecting its instability compared to hydromagnesite and therefore its higher solubility product. Using our dypingite and nesquehonite solubility products, it can be shown that hydromagnesite is more stable than both of these phases across a broad range of pH and pCO_2 conditions (Fig. 6). However, the relative stability of dypingite and nesquehonite is sensitive to pH for a fixed DIC concentration (Fig. 6). At higher pH there is a greater difference in their relative stability, with dypingite being more stable than nesquehonite, whereas a smaller difference is predicted at low pH, owing to the sensitivity of the dypingite solubility product to the activity of OH^- (Fig. 6).

4.2. Implications

Dypingite and nesquehonite are common weathering products of ultramafic rock (Beinlich and Austrheim, 2012; Garcia del Real et al., 2016; Lin et al., 2017; Power et al., 2007; Wilson et al., 2006, 2009a, b, 2014), and are documented CO_2 sinks that can be used to store CO_2 (Assima et al., 2012, 2014c; Bea et al., 2012; Gras et al., 2017; Hamilton et al., 2016, 2018; Harrison et al., 2013a, 2015, 2016, 2017; McCutcheon et al., 2014; Morgan et al., 2015; Power et al., 2007, 2013a, b, c, 2016; Pronost et al., 2011; Wilson et al., 2014). Yet, a lack of dypingite solubility data has hindered the ability to evaluate and predict its formation (Harrison et al., 2013a; Mavromatis et al., 2012; McCutcheon et al., 2014; Power et al., 2007, 2013c, 2014b; Wilson et al., 2010). The results presented in this study allow better estimation of dypingite stability in aqueous solution. For example, the solubility products determined in this study were added to PHREEQC V3 and used to calculate the dypingite saturation state in a previous experimental study in which it formed (Mavromatis et al., 2012), and in a natural wetland in Atlin, Canada, where it has been observed to form in

Table 4
Calculated saturation indices for nesquehonite and dypingite from an experimental study (Mavromatis et al., 2012) and a natural Mg-rich wetland (Power et al., 2014a, b).

Mg-carbonate precipitation experiments (data from Mavromatis et al., 2012)				
Experiment	Experiment type	Precipitated mineral	Saturation index	
			nesquehonite	dypingite
Abio-A-1	Abiotic	Nesquehonite	-0.51	-2.02
Abio-A-5	Abiotic	Dypingite	-0.15	1.24
Abio-A-10	Abiotic	Dypingite	-0.33	0.47
Abio-A-13	Abiotic	Dypingite	-0.16	1.34
Abio-B-18	Abiotic	Nesquehonite	0.04	2.70
Abio-C-7	Abiotic	Nesquehonite	0.10	1.99
Abio-C-9	Abiotic	Nesquehonite	0.10	2.05
Abio-C-11	Abiotic	Nesquehonite	0.05	1.93
Abio-C-12	Abiotic	Nesquehonite	0.13	2.79
Abio-D1-8	Abiotic	Nesquehonite	-0.01	2.26
Abio-D1-18	Abiotic	Nesquehonite	-0.05	2.37
Abio-D2-8	Abiotic	Dypingite	-0.04	1.99
Abio-D2-23	Abiotic	Dypingite	-0.26	0.81
Abio-E-7	Abiotic	Nesquehonite	0.05	2.35
Abio-E-10	Abiotic	Nesquehonite	0.06	2.44
Abio-E-11	Abiotic	Nesquehonite	0.11	2.58
Abio-E-13	Abiotic	Nesquehonite	0.14	2.77
Bio-A-1	Biotic	Nesquehonite	-0.44	-1.54
Bio-A-5	Biotic	Dypingite	0.14	3.21
Bio-A-8	Biotic	Dypingite	-0.18	1.86
Bio-A-12	Biotic	Dypingite	-0.64	1.53
Bio-A-15	Biotic	Dypingite	-0.81	0.63
Bio-B-4	Biotic	Nesquehonite	0.17	3.93
Bio-B-6	Biotic	Nesquehonite	0.09	3.72
Bio-B-8	Biotic	Nesquehonite	0.08	3.47
Bio-B-9	Biotic	Nesquehonite	0.08	3.56
Bio-B-10	Biotic	Nesquehonite	0.04	2.94
Bio-B-11	Biotic	Dypingite	-0.14	1.74
Bio-C-5	Biotic	Dypingite	-0.38	1.73
Bio-D-3	Biotic	Dypingite	-0.48	1.67
Bio-E-7	Biotic	Nesquehonite + Dypingite	0.07	2.48
Bio-E-9	Biotic	Nesquehonite + Dypingite	0.01	2.23
Bio-F-9	Biotic	Nesquehonite	0.02	2.07
Bio-G-2	Biotic	Nesquehonite	0.18	2.60
Bio-G-6	Biotic	Nesquehonite	-0.04	3.24
Bio-I-5	Biotic	Nesquehonite	0.10	2.53

Natural wetland (data from Power et al., 2014a, b)				
Location	Precipitation circumstances	Precipitated mineral	Saturation index	
			nesquehonite	dypingite[a]
Atlin, North lobe of main wetland	microbial mats	Dypingite	-0.07	0.40
Atlin, South lobe of main wetland	microbial mats	Dypingite	-0.12	0.09

[a] temperature of wetland water was 10°C, but dypingite K_{sp} used was for 25°C.

microbial mats (Power et al., 2007, 2009, 2014b). In the experimental study (Mavromatis et al., 2012), dypingite was somewhat supersaturated, suggesting that despite forming more readily at low temperature than hydromagnesite, its precipitation is nevertheless somewhat kinetically inhibited (Table 4). In the natural wetlands, where dypingite has both been directly observed as well as precipitated in experiments using water from the wetlands (Power et al., 2007, 2014b), dypingite was very close to equilibrium (Table 4), providing confidence in our K_{sp}^{dyp}. The K_{sp}^{dyp} determined in the present study can therefore be used to better constrain the possibility of dypingite precipitation in natural environments, and during engineered CO_2 storage operations. Note also that the nesquehonite solubility products in the PHREEQC databases appear to underestimate the stability of this mineral compared to the results of recent studies (this study; Wang and Li, 2012), and may thus underestimate its likelihood to form.

The main goal of engineered CO_2 storage operations is to ensure CO_2 is stored in a stable form and will not be substantially released over thousand-year timescales. Therefore, the design of CO_2 storage strategies to produce stable carbonate minerals is a key consideration, and has motivated numerous studies on the relative stability of Mg-carbonate minerals (Ballirano et al., 2010, 2013; Frost et al., 2008; Hales et al., 2008; Hänchen et al., 2008; Hopkinson et al., 2008; Hopkinson et al., 2012; Jauffret et al., 2015; Königsberger et al., 1999; Kristova et al., 2014; Lanas and Alvarez, 2004; Morgan et al., 2015; Vágvölgyi et al., 2008). The stoichiometry of minerals in terms of their Mg:C ratios and Mg:H_2O ratios also governs the efficiency of CO_2 sequestration; a Mg:C ratio of 1:1 such as provided by nesquehonite, lansfordite [$MgCO_3 \cdot 5H_2O$], and magnesite is most efficient. In dry conditions, such as in subaerially stored ultramafic mining wastes (Bea et al., 2012; Wilson et al., 2014), or near the injection of supercritical CO_2 in the subsurface (Chaka et al., 2016; Schaef et al., 2011, 2013), the availability of water may be a limiting factor for carbonate precipitation (Harrison et al., 2015, 2016; Schaef et al., 2011, 2013), therefore carbonates that consume less water during their formation,

such as dypingite, hydromagnesite, and magnesite, are desirable. The anhydrous carbonate, magnesite, is the ideal carbon sink in terms of stability, water requirements, and efficiency (Power et al., 2017). However, as it does not tend to form at low temperatures (Hänchen et al., 2008; Saldi et al., 2012), the hydrated carbonates are the targets for near Earth's surface temperature carbon storage. Although nesquehonite tends to precipitate from CO_2-rich solutions and under evaporative conditions (Harrison et al., 2013a; Königsberger et al., 1999; Power et al., 2007; Zhao et al., 2010), it readily transforms on hour- to month-long time scales to either dypingite or hydromagnesite, depending on the temperature. This transformation is accompanied by a slight loss of CO_2 to solution, as documented in the experiments at 25 °C and 35 °C (Fig. 4c and f), which is less ideal for CO_2 storage. On the other hand, the transformation from dypingite to the more stable phase, hydromagnesite, does not result in a loss of CO_2 (Ballirano et al., 2013), therefore this mineral phase transformation minimizes loss of stored CO_2. This suggests dypingite is a good target mineral for CO_2 storage at low temperatures. The tendency for dypingite to form over nesquehonite at atmospheric pCO_2 (~400 ppm), suggests that air capture coupled with carbonate mineral precipitation inherently produces a CO_2 sink of higher stability, though the relatively low concentration of CO_2 in ambient air compared to CO_2 point sources means that carbon mineralization rates can be limited by the availability of CO_2 (Bea et al., 2012; Harrison et al., 2013b; Pronost et al., 2012; Wilson et al., 2010, 2014). Microbially-mediated carbonate precipitation also tends to favor dypingite precipitation (Mavromatis et al., 2012; McCutcheon et al., 2016; Power et al., 2007), highlighting that microbially-mediated carbonation is a highly promising strategy for carbon mineralization at near Earth's surface conditions.

Ultramafic rock such as serpentinite contributes disproportionately to the release of chromium globally during natural weathering processes compared to other rock-types, owing to its high reactivity and high chromium content (Beinlich et al., 2018; McClain and Maher, 2016). It has recently been observed that secondary Mg-carbonate minerals formed during the weathering of ultramafic rock can help to mitigate the release of metals such as chromium, due both to incorporation of the metals into the carbonate minerals, and trapping of particulates within carbonate cement (Hamilton et al., 2016, 2018). The relative stability and mechanism of phase transformations is highly relevant to the cycling of potential contaminants like chromium in both natural and engineered ultramafic weathering environments. The change in mineral structure between nesquehonite and dypingite, and the alteration of crystal morphology during the phase transformation is indicative of a dissolution-reprecipitation process. This implies that metals initially stored in nesquehonite may be released to solution, and may or may not be equally reincorporated into dypingite, depending on the relative affinity for metals between the two phases. Similarly, isotopic signatures, which can be used as tracers for CO_2 cycling in natural ultramafic environments and mine wastes (Beinlich and Austrheim, 2012; Falk et al., 2016; Gras et al., 2017; Harrison et al., 2013a, 2016; Mavromatis et al., 2015; Mervine et al., 2014; Oelkers et al., 2018; Oskierski et al., 2013, 2016; Power et al., 2007; Shirokova et al., 2013; Wilson et al., 2009a, 2010, 2011, 2014), may be reset during mineral phase transformations that occur via dissolution-reprecipitation, complicating their interpretation.

5. Conclusions

The hydrated Mg-carbonate minerals nesquehonite and dypingite are common products of natural and engineered ultramafic rock weathering, and are of interest owing to their capacity to securely store atmospheric CO_2. Knowledge of their stability, longevity, and consequences of transformations will aid in our ability to ascertain the longevity and capacity of engineered carbon storage operations. In this study, the solubility of nesquehonite was re-examined, and the solubility of dypingite was measured for the first time. Our nesquehonite solubility product is in good agreement with the recent modeling study of Wang and Li (2012), which considered aqueous speciation. Our dypingite solubility product, though complicated by the presence of multiple dypingite-like phases, nevertheless allows estimation of dypingite saturation state in natural waters and engineered CO_2 storage operations. A natural wetland where dypingite has been observed (Power et al., 2007, 2009, 2014a, b) is demonstrated to be close to equilibrium with respect to dypingite, providing confidence in our values. Finally, our experimental results indicate that nesquehonite, which tends to form at greater than atmospheric pCO_2, can rapidly transform to dypingite at 25 °C and 35 °C, resulting in greater security of CO_2 storage due the higher stability of this phase, but accompanied by a slight loss of CO_2 to solution. This phase transformation apparently occurs via a dissolution re-precipitation mechanism, altering external crystal morphology, potentially releasing trace metals, and likely resetting isotopic signatures.

Acknowledgments

This research was funded by a Marie Skłowdowska-Curie Individual Fellowship awarded to ALH under grant agreement number 701478 (DryMIN) under the European Union's Horizon 2020 program, and partly by a postdoctoral fellowship from the Natural Sciences and Engineering Research Council of Canada. This study also benefited from the financial support of the ISIFoR Carnot institute (Institute for the Sustainable Engineering of Fossil Resources) under the project SERPCARB AAP-2016. The manuscript was improved by suggestions from two anonymous reviewers. Michel Thibaut and Ludovic Menjot are thanked for their assistance with XRD. We appreciate the assistance of Thierry Aigouy, Stephane Le Blond du Plouy, and James Davy with SEM, and of Carole Causserand with analyses of fluids. Andrew Thomson is thanked for access to and assistance with FTIR, which was supported by the Science and Technology Facilities Council under grant number ST/K000934/1. Alain Castillo is thanked for his assistance with laboratory apparatus and Sasha Wilson for valuable advice regarding XRD data. Ian Power generously provided fluid compositions for the wetland in Atlin, Canada [1].

Appendix A. Supplementary data

Supplementary data to this article can be found online at https://doi.org/10.1016/j.chemgeo.2018.11.003.

References

Assima, G.P., Larachi, F., Beaudoin, G., Molson, J., 2012. CO_2 sequestration in chrysotile mining residues—implication of watering and passivation under environmental conditions. Ind. Eng. Chem. Res. 51, 8726–8734.

Assima, G.P., Larachi, F., Molson, J., Beaudoin, G., 2014a. Comparative study of five Québec ultramafic mining residues for use in direct ambient carbon dioxide mineral sequestration. Chem. Eng. J. 245, 56–64.

Assima, G.P., Larachi, F., Molson, J., Beaudoin, G., 2014b. Emulation of ambient carbon dioxide diffusion and carbonation within nickel mining residues. Miner. Eng. 59, 39–44.

Assima, G.P., Larachi, F., Molson, J., Beaudoin, G., 2014c. Impact of temperature and oxygen availability on the dynamics of ambient CO_2 mineral sequestration by nickel mining residues. Chem. Eng. J. 240, 394–403.

Ballirano, P., De Vito, C., Ferrini, V., Mignardi, S., 2010. The thermal behaviour and structural stability of nesquehonite, $MgCO_3{\cdot}3H_2O$, evaluated by in situ laboratory parallel-beam X-ray powder diffraction: New constraints on CO_2 sequestration within minerals. J. Hazard. Mater. 178, 522–528.

Ballirano, P., De Vito, C., Mignardi, S., Ferrini, V., 2013. Phase transitions in the Mg-CO_2-H_2O system and the thermal decomposition of dypingite, $Mg_5(CO_3)_4(OH)_2{\cdot}5H_2O$: implications for geosequestration of carbon dioxide. Chem. Geol. 340, 59–67.

Bea, S.A., Wilson, S.A., Mayer, K.U., Dipple, G.M., Power, I.M., Gamazo, P., 2012. Reactive transport modeling of natural carbon sequestration in ultramafic mine tailings. Vadose Zone J. 11.

Beinlich, A., Austrheim, H., 2012. In situ sequestration of atmospheric CO_2 at low temperature and surface cracking of serpentinized peridotite in mine shafts. Chem. Geol. 332–333, 32–44.

Beinlich, A., Austrheim, H., Mavromatis, V., Grguric, B., Putnis, C.V., Putnis, A., 2018. Peridotite weathering is the missing ingredient of Earth's continental crust

composition. Nat. Commun. 9, 634.
Bénézeth, P., Saldi, G.D., Dandurand, J.L., Schott, J., 2011. Experimental determination of the solubility product of magnesite at 50 to 200 °C. Chem. Geol. 286, 21–31.
Bénézeth, P., Berninger, U.-N., Bovet, N., Schott, J., Oelkers, E.H., 2018. Experimental determination of the solubility product of dolomite at 50 to 253 °C. Geochim. Cosmochim. Acta 224, 262–275.
Berninger, U.N., Jordan, G., Schott, J., Oelkers, E.H., 2014. The experimental determination of hydromagnesite precipitation rates at 22.5–75 °C. Mineral. Mag. 78, 1405–1416.
Boschi, C., Dini, A., Dallai, L., Ruggieri, G., Gianelli, G., 2009. Enhanced CO_2-mineral sequestration by cyclic hydraulic fracturing and Si-rich fluid infiltration into serpentinites at Malentrata (Tuscany, Italy). Chem. Geol. 265, 209–226.
Brown, P.L., Drummond, S.E., Palmer, D.A., 1996. Hydrolysis of magnesium(II) at elevated temperatures. J. Chem. Soc. Dalton Trans. 14, 3071–3075.
Canterford, J.H., Tsambourakis, G., Lambert, B., 1984. Some observations on the properties of dypingite, $Mg_5(CO_3)_4(OH)_2{\cdot}5H_2O$, and related minerals. Mineral. Mag. 48, 437–442.
Chaka, A.M., Felmy, A.R., Qafoku, O., 2016. Ab initio thermodynamics of magnesium carbonates and hydrates in water-saturated supercritical CO_2 and CO_2-rich regions. Chem. Geol. 434, 1–11.
Cheng, W., Li, Z., 2009. Precipitation of nesquehonite from homogeneous supersaturated solutions. Cryst. Res. Technol. 44, 937–947.
Cheng, W., Li, Z., 2010. Nucleation kinetics of nesquehonite ($MgCO_3{\cdot}3H_2O$) in the $MgCl_2$-Na_2CO_3 system. J. Cryst. Growth 312, 1563–1571.
Cheng, W., Li, Z., Demopoulos, G.P., 2009. Effects of temperature on the preparation of magnesium carbonate hydrates by reaction of $MgCl_2$ with Na_2CO_3. Chin. J. Chem. Eng. 17, 661–666.
Davies, P.J., Bubela, B., 1973. The transformation of nesquehonite into hydromagnesite. Chem. Geol. 12, 289–300.
Ding, W., Ouyang, J., Yang, H., 2016. Synthesis and characterization of nesquehonite ($MgCO_3{\cdot}3H_2O$) powders from natural talc. Powder Technol. 292, 169–175.
Dong, M., Cheng, W., Li, Z., Demopoulos, G.P., 2008. Solubility and stability of nesquehonite ($MgCO_3{\cdot}H_2O$) in mixed NaCl + $MgCl_2$, NH_4Cl + $MgCl_2$, LiCl, and LiCl + $MgCl_2$ solutions. J. Chem. Eng. Data 53, 2586–2593.
Dong, M., Li, Z., Mi, J., Demopoulos, G.P., 2009. Solubility and stability of nesquehonite ($MgCO_3{\cdot}3H_2O$) in mixed NaCl + $MgCl_2$, NH_4Cl + $MgCl_2$, LiCl, and LiCl + $MgCl_2$ solutions. J. Chem. Eng. Data 54, 3002–3007.
Falk, E.S., Guo, W., Paukert, A.N., Matter, J.M., Mervine, E.M., Kelemen, P.B., 2016. Controls on the stable isotope compositions of travertine from hyperalkaline springs in Oman: Insights from clumped isotope measurements. Geochim. Cosmochim. Acta 192, 1–28.
Felmy, A.R., Qafoku, O., Arey, B.W., Hu, J.Z., Hu, M., Todd, Schaef H., Ilton, E.S., Hess, N.J., Pearce, C.I., Feng, J., Rosso, K.M., 2012. Reaction of water-saturated supercritical CO_2 with forsterite: evidence for magnesite formation at low temperatures. Geochim. Cosmochim. Acta 91, 271–282.
Frost, R.L., Palmer, S.J., 2011. Infrared and infrared emission spectroscopy of nesquehonite $Mg(OH)(HCO_3){\cdot}2H_2O$-implications for the formula of nesquehonite. Spectrochim. Acta A Mol. Biomol. Spectrosc. 78, 1255–1260.
Frost, R.L., Bahfenne, S., Graham, J., Martens, W.N., 2008. Thermal stability of artinite, dypingite and brugnatellite—implications for the geosequestration of green house gases. Thermochim. Acta 475, 39–43.
Garcia del Real, P.G., Maher, K., Kluge, T., Bird, D.K., Brown, G.E., John, C.M., 2016. Clumped-isotope thermometry of magnesium carbonates in ultramafic rocks. Geochim. Cosmochim. Acta 193, 222–250.
Gautier, Q., Bénézeth, P., Mavromatis, V., Schott, J., 2014. Hydromagnesite solubility product and growth kinetics in aqueous solution from 25 to 75 °C. Geochim. Cosmochim. Acta 138, 1–20.
Gerdemann, S.J., O'Connor, W.K., Dahlin, D.C., Penner, L.R., Rush, H., 2007. Ex situ aqueous mineral carbonation. Environ. Sci. Technol. 41, 2587–2593.
Gislason, S.R., Oelkers, E.H., 2014. Carbon storage in basalt. Science 344, 373–374.
Gras, A., Beaudoin, G., Molson, J., Plante, B., Bussière, B., Lemieux, J.M., Dupont, P.P., 2017. Isotopic evidence of passive mineral carbonation in mine wastes from the Dumont Nickel Project (Abitibi, Quebec). Int. J. Greenhouse Gas Control 60, 10–23.
Hales, M., Frost, R., Martens, W., 2008. Thermo-Raman spectroscopy of synthetic nesquehonite - implication for the geosequestration of greenhouse gases. J. Raman Spectrosc. 38, 1141–1149.
Hamilton, J.L., Wilson, S.A., Morgan, B., Turvey, C.C., Paterson, D.J., MacRae, C., McCutcheon, J., Southam, G., 2016. Nesquehonite sequesters transition metals and CO_2 during accelerated carbon mineralisation. Int. J. Greenhouse Gas Control 55, 73–81.
Hamilton, J.L., Wilson, S.A., Morgan, B., Turvey, C.C., Paterson, D.J., Jowitt, S.M., McCutcheon, J., Southam, G., 2018. Fate of transition metals during passive carbonation of ultramafic mine tailings via air capture with potential for metal resource recovery. Int. J. Greenhouse Gas Control 71, 155–167.
Hänchen, M., Prigiobbe, V., Baciocchi, R., Mazzotti, M., 2008. Precipitation in the Mg-carbonate system—effects of temperature and CO_2 pressure. Chem. Eng. Sci. 63, 1012–1028.
Harrison, A.L., Power, I.M., Dipple, G.M., 2013a. Accelerated carbonation of brucite in mine tailings for carbon sequestration. Environ. Sci. Technol. 47, 126–134.
Harrison, A.L., Power, I.M., Dipple, G.M., 2013b. Strategies for enhancing carbon sequestration in Mg-rich mine tailings. In: Brown, A., Figueroa, L., Wolkersdorfer, C. (Eds.), Reliable Mine Water Technology. Vol. 1. Publication Printers, Denver, Colorado, USA, pp. 593–598.
Harrison, A.L., Dipple, G.M., Power, I.M., Mayer, K.U., 2015. Influence of surface passivation and water content on mineral reactions in unsaturated porous media: Implications for brucite carbonation and CO_2 sequestration. Geochim. Cosmochim. Acta 148, 477–495.
Harrison, A.L., Dipple, G.M., Power, I.M., Mayer, K.U., 2016. The impact of evolving mineral-water-gas interfacial areas on mineral-fluid reaction rates in unsaturated porous media. Chem. Geol. 421, 65–80.
Harrison, A.L., Dipple, G.M., Song, W., Power, I.M., Mayer, K.U., Beinlich, A., Sinton, D., 2017. Changes in mineral reactivity driven by pore fluid mobility in partially wetted porous media. Chem. Geol. 463, 1–11.
Hartmann, J., West, J., Renforth, P., Kohler, P., De La Rocha, C., Wolf-Gladrow, D.A., Durr, H., Scheffran, J., 2013. Enhanced chemical weathering as a geoengineering strategy to reduce atmospheric carbon dioxide, a nutrient source and to mitigate ocean acidification. Rev. Geophys. 51, 113–149.
Helgeson, H.C., 1969. Thermodynamics of hydrothermal systems at elevated temperatures and pressures. Am. J. Sci. 267, 729–804.
Highfield, J., Chen, J., Haghughatlari, M., Abacka, J., Zevenhoven, R., 2016. Low-temperature gas-solid carbonation of magnesia and magnesium hydroxide promoted by non-immersive contact with water. RSC Adv. 6, 89655–89664.
Hopkinson, L., Rutt, K., Cressey, G., 2008. The transformation of nesquehonite to hydromagnesite in the system CaO-MgO-H_2O-CO_2: an experimental spectroscopic study. J. Geol. 116, 387–400.
Hopkinson, L., Kristova, P., Rutt, K., Cressey, G., 2012. Phase transitions in the system MgO – CO_2 – H_2O during CO_2 degassing of Mg-bearing solutions. Geochim. Cosmochim. Acta 76, 1–13.
Hostetler, P., 1964. The degree of saturation of magnesium and calcium carbonate minerals in natural waters. Int. Assoc. Sci. Hydrol. 64, 34–49.
Hövelmann, J., Putnis, C.V., Ruiz-Agudo, E., Austrheim, H., 2012. Direct nanoscale observations of CO_2 sequestration during brucite [$Mg(OH)_2$] dissolution. Environ. Sci. Technol. 46, 5253–5260.
Jauffret, G., Morrison, J., Glasser, F.P., 2015. On the thermal decomposition of nesquehonite. J. Therm. Anal. Calorim. 5–10.
Kazakov, A.V., Tikhomirova, M.M., Plotnikova, V.I., 1959. The system of carbonate equilibria. Int. Geol. Rev. 1, 1–39.
Kelemen, P.B., Matter, J., 2008. In situ carbonation of peridotite for CO_2 storage. Proc. Natl. Acad. Sci. 105, 17295–17300.
Kline, W., 1929. The solubility of magnesium carbonate (nesquehonite) in water at 25° and pressures of carbon dioxide up to one atmosphere. J. Am. Chem. Soc. 51, 2093–2097.
Königsberger, E., Königsberger, L.-C., Gamsjäger, H., 1999. Low-temperature thermodynamic model for the system Na_2CO_3-$MgCO_3$-$CaCO_3$-H_2O. Geochim. Cosmochim. Acta 63, 3105–3119.
Kristova, P., Hopkinson, L.J., Rutt, K.J., Hunter, H.M.A., Cressey, G., 2014. Carbonate mineral paragenesis and reaction kinetics in the system MgO–CaO–CO_2–H_2O in presence of chloride or nitrate ions at near surface ambient temperatures. Appl. Geochem. 50, 16–24.
Lackner, K.S., 2003. A Guide to CO_2 Sequestration. Science 300, 1677–1678.
Lackner, K.S., Wendt, C.H., Butt, D.P., Joyce, E.L., Sharp, D.H., 1995. Carbon dioxide disposal in carbonate minerals. Energy 20, 1153–1170.
Lanas, J., Alvarez, J.I., 2004. Dolomitic lime: thermal decomposition of nesquehonite. Thermochim. Acta 421, 123–132.
Langmuir, D., 1965. Stability of carbonates in the system MgO-CO_2-H_2O. J. Geol. 73, 730–754.
Lin, Y., Zheng, M., Ye, C., 2017. Hydromagnesite precipitation in the alkaline lake Dujiali, central Qinghai-Tibetan Plateau: Constraints on hydromagnesite precipitation from hydrochemistry and stable isotopes. Appl. Geochem. 78, 139–148.
Loring, J.S., Thompson, C.J., Zhang, C., Wang, Z., Schaef, H.T., Rosso, K.M., 2012. In situ infrared spectroscopic study of brucite carbonation in dry to water-saturated supercritical carbon dioxide. J. Phys. Chem. A 116, 4768–4777.
Marion, G., 2001. Carbonate mineral solubility at low temperatures in the Na-K-Mg-Ca-H-Cl-SO_4-OH-HCO_3-CO_3-CO_2-H_2O system. Geochim. Cosmochim. Acta 65, 1883–1896.
Matter, J., Stute, M., Snæbjörnsdottir, S.Ó., Oelkers, E., Gislason, S.R., Aradottir, E.S., Sigfusson, B., Gunnarsson, I., Alfredsson, H.A., Wolff-boenisch, D., Mesfin, K., Fernandez de la Reguera Taya, D., Hall, J., Dideriksen, K., Broecker, W.S., 2016. Rapid carbon mineralization for permanent disposal of anthropogenic carbon dioxide emissions. Science 352, 1312–1314.
Mavromatis, V., Pearce, C.R., Shirokova, L.S., Bundeleva, I.A., Pokrovsky, O.S., Bénézeth, P., Oelkers, E.H., 2012. Magnesium isotope fractionation during hydrous magnesium carbonate precipitation with and without cyanobacteria. Geochim. Cosmochim. Acta 76, 161–174.
Mavromatis, V., Bundeleva, I.A., Shirokova, L.S., Millo, C., Pokrovsky, O.S., Bénézeth, P., Ader, M., Oelkers, E.H., 2015. The continuous re-equilibration of carbon isotope compositions of hydrous Mg carbonates in the presence of cyanobacteria. Chem. Geol. 404, 41–51.
McClain, C.N., Maher, K., 2016. Chromium fluxes and speciation in ultramafic catchments and global rivers. Chem. Geol. 426, 135–157.
McCutcheon, J., Power, I.M., Harrison, A.L., Dipple, G.M., Southam, G., 2014. A greenhouse-scale photosynthetic microbial bioreactor for carbon sequestration in magnesium carbonate minerals. Environ. Sci. Technol. 48, 9142–9151.
McCutcheon, J., Wilson, S.A., Southam, G., 2016. Microbially accelerated carbonate mineral precipitation as a strategy for in situ carbon sequestration and rehabilitation of asbestos mine sites. Environ. Sci. Technol. 50, 1419–1423.
McCutcheon, J., Turvey, C.C., Wilson, S.A., Hamilton, J.L., Southam, G., 2017. Experimental deployment of microbial mineral carbonation at an asbestos mine: potential applications to carbon storage and tailings stabilization. Minerals 7, 15–18.
Mervine, E.M., Humphris, S.E., Sims, K.W.W., Kelemen, P.B., Jenkins, W.J., 2014. Carbonation rates of peridotite in the Samail Ophiolite, Sultanate of Oman, constrained through 14C dating and stable isotopes. Geochim. Cosmochim. Acta 126, 371–397.

Montes-Hernandez, G., Renard, F., Chiriac, R., Findling, N., Toche, F., 2012. Rapid precipitation of magnesite microcrystals from $Mg(OH)_2$ - H_2O - CO_2 slurry enhanced by NaOH and a heat-aging step (from ~20 to 90 °C). Cryst. Growth Des. 12, 5233–5240.
Montserrat, F., Renforth, P., Hartmann, J., Knops, P., Leermakers, M., Meysman, F.J.R., 2017. Olivine dissolution in seawater: implications for CO_2 sequestration through enhanced weathering in coastal environments. Environ. Sci. Technol. 51, 3960–3972.
Morgan, B., Wilson, S.A., Madsen, I.C., Gozukara, Y.M., Habsuda, J., 2015. Increased thermal stability of nesquehonite ($MgCO_3{\cdot}3H_2O$) in the presence of humidity and CO_2: implications for low-temperature CO_2 storage. Int. J. Greenhouse Gas Control 39, 366–376.
Oelkers, E.H., Cole, D.R., 2008. Carbon dioxide sequestration: a solution to a global problem. Elements 4, 305–310.
Oelkers, E.H., Berninger, U.N., Perez-Fernandez, A., Chmeleff, J., Mavromatis, V., 2018. The temporal evolution of magnesium isotope fractionation during hydromagnesite dissolution, precipitation, and at equilibrium. Geochim. Cosmochim. Acta 226, 36–49.
Oskierski, H.C., Dlugogorski, B.Z., Jacobsen, G., 2013. Sequestration of atmospheric CO_2 in chrysotile mine tailings of the Woodsreef Asbestos Mine, Australia: quantitative mineralogy, isotopic fingerprinting and carbonation rates. Chem. Geol. 358, 156–169.
Oskierski, H.C., Dlugogorski, B.Z., Oliver, T.K., Jacobsen, G., 2016. Chemical and isotopic signatures of waters associated with the carbonation of ultramafic mine tailings, Woodsreef Asbestos Mine, Australia. Chem. Geol. 436, 11–23.
Palmer, D.A., Wesolowski, D.J., 1997. Potentiometric measurements of the first hydrolysis quotient of magnesium (II) to 250 °C and 5 molal ionic strength (NaCl). J. Solut. Chem. 26, 2167–2232.
Parkhurst, D.L., Appelo, C.A.J., 2013. Description of input and examples for PHREEQC version 3 — a computer program for speciation, batch-reaction, one-dimensional transport, and inverse geochemical calculations. In: U.S. Geological Survey Techniques and Methods, Book 6, Chap. A43, 497 p. Denver, Colorado, pp. 497.
Patterson, C.S., Slocum, G.H., Busey, R.H., Mesmer, R.E., 1982. Carbonate equilibria in hydrothermal systems: first ionization of carbonic acid in NaCl media to 300 °C. Geochim. Cosmochim. Acta 46, 1653–1663.
Patterson, C.S., Busey, R.H., Mesmer, R.E., 1984. Second ionization of carbonic acid in NaCl media to 250 °C. J. Solut. Chem. 13, 647–661.
Power, I.M., Wilson, S.A., Thom, J.M., Dipple, G.M., Southam, G., 2007. Biologically induced mineralization of dypingite by cyanobacteria from an alkaline wetland near Atlin, British Columbia, Canada. Geochem. Trans. 8, 13.
Power, I.M., Wilson, S.A., Thom, J.M., Dipple, G.M., Gabites, J.E., Southam, G., 2009. The hydromagnesite playas of Atlin, British Columbia, Canada: a biogeochemical model for CO_2 sequestration. Chem. Geol. 260, 286–300.
Power, I.M., Dipple, G.M., Southam, G., 2010. Bioleaching of ultramafic tailings by *Acidithiobacillus* spp. for CO_2 sequestration. Environ. Sci. Technol. 44, 456–462.
Power, I.M., Harrison, A.L., Dipple, G.M., Wilson, S.A., Kelemen, P.B., Hitch, M., Southam, G., 2013a. Carbon mineralization: from natural analogues to engineered systems. Rev. Mineral. Geochem. 77, 305–360.
Power, I.M., Wilson, S.A., Dipple, G.M., 2013b. Serpentinite carbonation for CO_2 sequestration. Elements 9, 115–121.
Power, I.M., Harrison, A.L., Dipple, G.M., Southam, G., 2013c. Carbon sequestration via carbonic anhydrase facilitated magnesium carbonate precipitation. Int. J. Greenhouse Gas Control 16, 145–155.
Power, I.M., McCutcheon, J., Harrison, A.L., Wilson, S.A., Dipple, G.M., Kelly, S., Southam, C., Southam, G., 2014a. Strategizing carbon-neutral mines: a case for pilot projects. Minerals 4, 399–436.
Power, I.M., Wilson, S.A., Harrison, A.L., Dipple, G.M., McCutcheon, J., Southam, G., Kenward, P.A., 2014b. A depositional model for hydromagnesite-magnesite playas near Atlin, British Columbia, Canada. Sedimentology 61, 1701–1733.
Power, I.M., Harrison, A.L., Dipple, G.M., 2016. Accelerating mineral carbonation using carbonic anhydrase. Environ. Sci. Technol. 50, 2610–2618.
Power, I.M., Kenward, P.A., Dipple, G.M., Raudsepp, M., 2017. Room temperature magnesite precipitation. Cryst. Growth Des. 17, 5652–5659.
Pronost, J., Beaudoin, G., Tremblay, J., Larachi, F., Duchesne, J., Hébert, R., Constantin, M., 2011. Carbon sequestration kinetic and storage capacity of ultramafic mining waste. Environ. Sci. Technol. 45, 9413–9420.
Pronost, J., Beaudoin, G., Lemieux, J.-M., Hebert, R., Constantin, M., Marcouiller, S., Klein, M., Duchesne, J., Molson, J.W., Larachi, F., Maldague, X., 2012. CO_2-depleted warm air venting from chrysotile milling waste (Thetford Mines, Canada): evidence for in-situ carbon capture from the atmosphere. Geology 40, 275–278.
Raade, G., 1970. Dypingite, a new hydrous basic carbonate of magnesium, from Norway. Am. Mineral. 55, 1457–1465.
Renforth, P., 2012. The potential of enhanced weathering in the UK. Int. J. Greenhouse Gas Control 10, 229–243.
Rigopoulos, I., Harrison, A.L., Delimitis, A., Ioannou, I., Efstathiou, A.M., Kyratsi, T., Oelkers, E.H., 2018. Carbon sequestration via enhanced weathering of peridotites and basalts in seawater. Appl. Geochem. 91, 197–207.
Robie, R.A., Hemingway, B.S., 1972. The heat capacities at low-temperatures and entropies at 298.15 K of nesquehonite, $MgCO_3{\cdot}3H_2O$, and hydromagnesite. Am. Mineral. 57, 1768–1781.
Robie, R., Hemingway, B., 1973. The enthalpies of formation of nesquehonite, $MgCO_3{\cdot}3H_2O$, and hydromagnesite, $5MgO{\cdot}4CO_2{\cdot}5H_2O$. J. Res. U. S. Geol. Surv. 1, 543–547.
Ruiz-Agudo, E., Putnis, C.V., Rodriguez-Navarro, C., Putnis, A., 2012. Mechanism of leached layer formation during chemical weathering of silicate minerals. Geology 40, 947–950.
Saldi, G.D., Jordan, G., Schott, J., Oelkers, E.H., 2009. Magnesite growth rates as a function of temperature and saturation state. Geochim. Cosmochim. Acta 73, 5646–5657.
Saldi, G.D., Schott, J., Pokrovsky, O.S., Gautier, Q., Oelkers, E.H., 2012. An experimental study of magnesite precipitation rates at neutral to alkaline conditions and 100–200 °C as a function of pH, aqueous solution composition and chemical affinity. Geochim. Cosmochim. Acta 83, 93–109.
Schaef, H.T., Windisch, C.F., McGrail, B.P., Martin, P.F., Rosso, K.M., 2011. Brucite [$Mg(OH_2)$] carbonation in wet supercritical CO_2: an in situ high pressure X-ray diffraction study. Geochim. Cosmochim. Acta 75, 7458–7471.
Schaef, H.T., Mcgrail, B.P., Loring, J.L., Bowden, M.E., Arey, B.W., Rosso, K.M., 2013. Forsterite [Mg_2SiO_4] carbonation in wet supercritical CO_2: an in situ high-pressure X-ray diffraction study. Environ. Sci. Technol. 47, 174–181.
Schuiling, R.D., Krijgsman, P., 2006. Enhanced weathering: An effective and cheap tool to sequester CO2. Clim. Chang. 74, 349–354.
Shirokova, L.S., Mavromatis, V., Bundeleva, I.A., Pokrovsky, O.S., Bénézeth, P., Gérard, E., Pearce, C.R., Oelkers, E.H., 2013. Using Mg isotopes to trace cyanobacterially mediated magnesium carbonate precipitation in alkaline lakes. Aquat. Geochem. 19, 1–24.
Shock, E.L., Helgeson, H.C., 1988. Calculation of the thermodynamic and transport properties of aqueous species at high pressures and temperatures: correlation algorithms for ionic species and equation of state predictions to 5 kb and 1000 °C. Geochim. Cosmochim. Acta 52, 2009–2036.
Shock, E.L., Sassani, D.C., Willis, M., Sverjensky, D.A., 1997. Inorganic species in geologic fluids: correlations among standard molal thermodynamic properties of aqueous ions and hydroxide complexes. Geochim. Cosmochim. Acta 61, 907–950.
Stefansson, A., Bénézeth, P., Schott, J., 2014. Potentiometric and spectrophotometric study of the stability of magnesium carbonate and bicarbonate pairs to 150C and aqueous inorganic carbon speciation and magnesite solubility. Geochim. Cosmochim. Acta 138, 21–31.
Sundquist, E.T., 1993. The global carbon dioxide budget. Science 259, 934–941.
Sutradhar, N., Sinhamahapatra, A., Pahari, S.K., Pal, P., Bajaj, H.C., Mukhopadhyay, I., Panda, A.B., 2011. Controlled synthesis of different morphologies of MgO and their use as solid base catalysts. J. Phys. Chem. C 115, 12308–12316.
Vágvölgyi, V., Hales, M., Frost, R.L., Locke, A., Kristóf, J., Horváth, E., 2008. Conventional and controlled rate thermal analysis of nesquehonite $Mg(HCO_3)(OH){\cdot}2(H_2O)$. J. Therm. Anal. Calorim. 94, 523–528.
Wagman, D.D., Evans, W.H., Parker, V.B., Schumm, R.H., Halow, I., Bailey, S.M., Churney, K.L., Nuttall, R.L., 1982. The NBS tables of chemical thermodynamic properties: selected values for inorganic and C1 and C2 organic substances in SI units. J. Chem. Ref. Data 392 (supplement n. 2), 11.
Wang, D., Li, Z., 2012. Chemical modeling of nesquehonite solubility in $Li + Na + K + NH_4 + Mg + Cl + H_2O$ System with a speciation-based approach. Chin. J. Chem. Eng. 20, 2670276.
Wang, Y., Li, Z., Demopoulos, G.P., 2008. Controlled Precipitation of Nesquehonite ($MgCO_3{\cdot}3H_2O$) by the Reaction of $MgCl_2$ With $(NH_4)_2CO_3$. pp. 1220–1227.
Wilson, S.A., Raudsepp, M., Dipple, G.M., 2006. Verifying and quantifying carbon fixation in minerals from serpentine-rich mine tailings using the Rietveld method with X-ray powder diffraction data. Am. Mineral. 91, 1331–1341.
Wilson, S.A., Dipple, G.M., Power, I.M., Thom, J.M., Anderson, R.G., Raudsepp, M., Gabites, J.E., Southam, G., 2009a. Carbon dioxide fixation within mine wastes of ultramafic-hosted ore deposits: examples from the Clinton Creek and Cassiar chrysotile deposits, Canada. Econ. Geol. 104, 95–112.
Wilson, S.A., Raudsepp, M., Dipple, G.M., 2009b. Quantifying carbon fixation in trace minerals from processed kimberlite: a comparative study of quantitative methods using X-ray powder diffraction data with applications to the Diavik Diamond Mine, Northwest Territories, Canada. Appl. Geochem. 24, 2312–2331.
Wilson, S.A., Barker, S.L.L., Dipple, G.M., Atudorei, V., 2010. Isotopic disequilibrium during uptake of atmospheric CO_2 into mine process waters: Implications for CO_2 sequestration. Environ. Sci. Technol. 44, 9522–9529.
Wilson, S.A., Dipple, G.M., Power, I.M., Barker, S.L.L., Fallon, S.J., Southam, G., 2011. Subarctic weathering of mineral wastes provides a sink for atmospheric CO_2. Environ. Sci. Technol. 45, 7727–7736.
Wilson, S.A., Harrison, A.L., Dipple, G.M., Power, I.M., Barker, S.L.L., Mayer, K.U., Fallon, S.J., Raudsepp, M., Southam, G., 2014. Offsetting of CO_2 emissions by air capture in mine tailings at the Mount Keith Nickel Mine, Western Australia: rates, controls and prospects for carbon neutral mining. Int. J. Greenhouse Gas Control 25, 121–140.
Xiong, Y., 2011. Experimental determination of solubility constant of hydromagnesite (5424) in NaCl solutions up to 4.4 m at room temperature. Chem. Geol. 284, 262–269.
Xiong, Y., Lord, A.S., 2008. Experimental investigations of the reaction path in the $MgO–CO_2–H_2O$ system in solutions with various ionic strengths, and their applications to nuclear waste isolation. Appl. Geochem. 23, 1634–1659.
Zhang, Z., Zheng, Y., Ni, Y., Liu, Z., Chen, J., Liang, X., 2006. Temperature- and pH-dependent morphology and FT-IR analysis of magnesium carbonate hydrates. J. Phys. Chem. B 110, 12969–12973.
Zhao, L., Sang, L., Chen, J., Ji, J., Teng, H.H., 2010. Aqueous carbonation of natural brucite: relevance to CO_2 sequestration. Environ. Sci. Technol. 44, 406–411.
Zhao, L., Zhu, C., Ji, J., Chen, J., Teng, H.H., 2013. Thermodynamic and kinetic effect of organic solvent on the nucleation of nesquehonite. Geochim. Cosmochim. Acta 106, 192–202.